Graduate School Form 30
Updated 1/15/2015

PURDUE UNIVERSITY
GRADUATE SCHOOL
Thesis/Dissertation Acceptance

This is to certify that the thesis/dissertation prepared

By Yuanzhi Cao

Entitled

THE DEVELOPMENT OF POLYSTYRENE BASED MICROFLUIDIC GAS GENERATION SYSTEM

For the degree of Master of Science in Mechanical Engineering

Is approved by the final examining committee:

Likun Zhu
Chair

Huidan Yu

Hazim El-Mounayri

To the best of my knowledge and as understood by the student in the Thesis/Dissertation Agreement, Publication Delay, and Certification Disclaimer (Graduate School Form 32), this thesis/dissertation adheres to the provisions of Purdue University's "Policy of Integrity in Research" and the use of copyright material.

Approved by Major Professor(s): Likun Zhu

Approved by: Sohel Anwar 4/17/2015

Head of the Departmental Graduate Program Date

THE DEVELOPMENT OF POLYSTYRENE BASED MICROFLUIDIC GAS GENERATION SYSTEM

A Thesis

Submitted to the Faculty

of

Purdue University

by

Yuanzhi Cao

In Partial Fulfillment of the

Requirements for the Degree

of

Master of Science in Mechanical Engineering

May 2015

Purdue University

Indianapolis, Indiana

For

my *mother*

and

my *wife*

ACKNOWLEDGMENTS

This work is supported by National Science Foundation under Grant No. 1264739. We would like to acknowledge the Integrated Nanosystems Development Institute (INDI) at IUPUI for use of their shared facilities (craft cutter, FESEM, etc.) in support of our research. We would also like to acknowledge the Molecular Structure Center at Indiana University Bloomington (IUB), and especially the XPS facility supervisor Dr. Yaroslav Lozovyy, for his help on our XPS experiments. Moreover, I want to specially thank the research scientist Dr. Sun Tao, at Advanced Photon Source (APS), Argonne National Laboratory, for his helpful guidance in my experiments as well as my future academic plans.

For those who constantly give me their assistance on a daily basis, I would like to first thank my academic advisor Dr. Likun Zhu, your rigorous attitude towards scientific research inspires me constantly.

Next, I would like to convey my gratitude to all the professors that have enlightened me. Your knowledge and wisdom guided me through this journey.

I would also like to thank my lab mates and group mates: CheolWoong Lim, Jacob Bontrager-Singer, Bo Yan, Zhibin Song, Rani Vijaya, and Yi Cui, for your help, encouragement, and accompany during this uneasy period of time.

Finally, I'd like to thank my family and my wife, your endless love and unconditional support is the very reason I can keep going forward.

TABLE OF CONTENTS

Page

LIST OF TABLES

LIST OF FIGURES

Figure Page

ABSTRACT

Cao, Yuanzhi. M.S.M.E., Purdue University, May 2015. The Development of Polystyrene Based Microfluidic Gas Generation System. Major Professor: Likun Zhu.

The purpose of this thesis is to use experimental methods to seek deeper understanding and better performance in the self-circulating self-regulating microfluidic gas generator initially developed in Dr. Zhu's group, by changing the major features and dimensions in the reaction channel of the device. In order to effectively conduct experiments described above, a microfabrication method that is capable of making new microfluidic devices with low cost, short time period, as well as relatively high accuracy was needed first. Developing such a fabrication method is the major part of this thesis. We initially used patterned polymer films and glass slide, and bonded them together by sequentially aligning and stacking them into a microfluidic device with patterned double-sided tapes. Later we developed a more advanced microfabrication method that used only patterned polystyrene (PS) films. The patterned PS films were obtained from a digital cutter and they were bonded into a microfluidic device by thermopress bonding method that required no heterogeneous bonding agents. This new method did not need manual assembly which greatly improved its precision (100 μm), and it used only PS as device material that has favorable surface wetting property for microfluidics applications.

In order to find the optimized microfluidic channel design to improve gas generating performance, we've designed and fabricated microfluidic devices with different channel dimensions using the PS fabrication method. Based on the gas generation testing results of those devices, we were able to come up with the optimal dimensions for the reaction channel that had the best gas generation performance.

To obtain a more fundamental understanding about the working mechanism of our device and its bubble dynamics, we have conducted ultrafast X-ray imaging test at Advanced Photon Source (APS), Argonne National Laboratory. High speed (100 KHz) phase contrast images were captured that allowed us to observe directly inside the reaction channel on the cross section view during the self-circulating catalytic reaction. The images provided us with lots of insightful information that in turn helped the dimensional improvement for the microchannel design. The 100 KHz high speed images also gave us useful information about the dynamics of bubble development on a catalyst bed, such as growth and merging of the bubbles.

1. INTRODUCTION

1.1 Thesis Background

The new research of micro scale power sources is constantly motivated by the fast growing portable electronics, such as mobile phones, laptop computers, digital cameras, global positioning system (GPS), personal digital assistants (PDA), etc. The goal of such small power source is high performance with reasonable long performing time. Rechargeable batteries in current market are under considerable pressure from customers' future requirements, especially when dealing with high power and energy density for micro scale systems. Researches and studies from the past decades showed that micro-hydrogen proton exchange membrane fuel cells have a promising chance to replace batteries in the future [1]. However, a lot of technology barriers have to be overcome before that can truly happen.

One of the many challenges about portable hydrogen-oxygen fuel cell is fuel storage, in this case, gas storage of hydrogen and oxygen. Taking hydrogen for example, it can be stored in various ways, such as compressed gas, liquid hydrogen, physical adsorption on metal organic frameworks [2] and metal or chemical hydrides [3]. But unfortunately, most of these gas storage methods are impractical for small portable power source applications such as micro fuel cell due to low energy density, complicated control units, relatively expensive cost, and the strict storage conditions [4].

Recent researches and studies lead the direction to an on-demand micro gas generation system which can store gas in aqueous chemical form and release it during controllable catalytic reaction. There are several advantages in such method: (1) The aqueous chemicals can be very stable under normal conditions, which means they are easy to store, (2) The aqueous chemicals that react to release gas with moderate concentration usually have a relatively high gas storage capacity, (3) The controlled

catalytic reaction has a very fast reaction rate which means the device will guarantee a high gas generation rate.

A lot of work has been done towards the direction. For example, Gervasio et al. [5] has reported their research work about a gas generator that operated at room temperature in 2002. Hoeppner et al. [6] has reported a sodium borohydride ($NaBH_4$), also known as SB solution, hydrogen micro-reactor assembly by glass stack bonding. In their work, an external liquid pump was used to pump the SB reactant solution into the catalytic reaction channel, a porous membrane then was used as a gas/liquid separation tool. The hydrogen generation rate was regulated by manually controlling the flow rate of the reactant over the catalyst layer. Strizki and Shah [7] have proposed a hydrogen generator with adjustable gas generation rate. In their invention, the gas generator regulated the gas generation rate by providing relative movement between fuel tank and the catalytic reaction chamber so as to increase or decrease the reaction rate. The relative movement provided was in response of monitoring the parameters of the gas generation process. Therefore, additional sensors and actuators were needed in their design.

Latest results by several research groups have unanimously reached an agreement that the future of such micro fuel cell integrated with a microfluidic gas generator lied in capillary driven self-circulation or self-pumping and self-regulation with no parasitic power consumption [8–13]. The on-demand hydrogen generation device designed and fabricated by the team of Dr. Zhu showed a notable advancement which had the capability of integrating self-circulation, self-regulation, gas/liquid separation, catalytic reaction and electrochemical reaction in the micro device [12]. The self-circulation system could pump the reactant solution into the reaction channel of the device to generate gas and form a circuit; the self-regulation system was capable of creating an on-demand feedback control of the reaction by modifying the reaction rate according to the output requirement; the gas/liquid separation was achieved using a hydrophobic nanoscale porous membrane; the reaction in the microfluidic channel and the fuel cell was enabled with highly porous structure catalyst material. This

design had shown great advantage for removing external auxiliary devices like liquid pumps, which not only optimized power utilization by eliminating parasitic power consumption, but also shrank the device scale for wider range of applications.

1.2 Principle Illustration

This thesis is based on the idea from the paper, "An on-demand microfluidic hydrogen generator with self-regulated gas generation and self-circulated reaction exchange with a rechargeable reservoir" presented by Dr. Likun Zhu's group in their previous research [12]. The working principle of the device is illustrated in Figure 1.1.

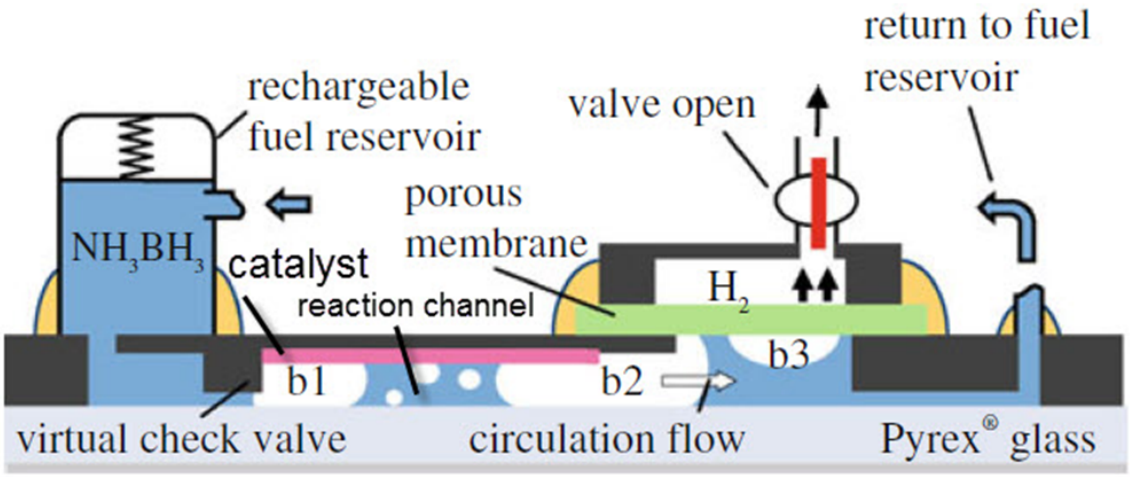

Fig. 1.1. Schematic of the microfluidic gas generation system.

According to gas generating requirement, different reactant solution was chosen. For example, NH_3BH_3 was used for hydrogen generation and H_2O_2 was used for oxygen generation, respectively. The reaction formulas are given as below:

$$HN_3BH_3 + 2H_2O \xrightarrow{Pt} NH_4^+ + BO_2^- + 3H_2 \uparrow \tag{1.1}$$

$$2H_2O_2 \xrightarrow{Pt} 2H_2O + O_2 \uparrow \tag{1.2}$$

When the reactant solution from the rechargeable fuel reservoir goes into the reaction channel through the left virtual check valve, reaction starts when it contacts the Pt catalyst layer. Therefore gas bubbles begins to generate near the virtual check valve, with the reaction goes on, the bubble (b1) expands bigger and bigger to both left and right directions almost evenly, because the capillary force applied to both meniscuses are nearly the same. However, when the bubble expands big enough that its left meniscus reaches the virtual check valve, the capillary force balance will be broken because of the significant dimensional difference between the virtual check valve and the reaction channel.

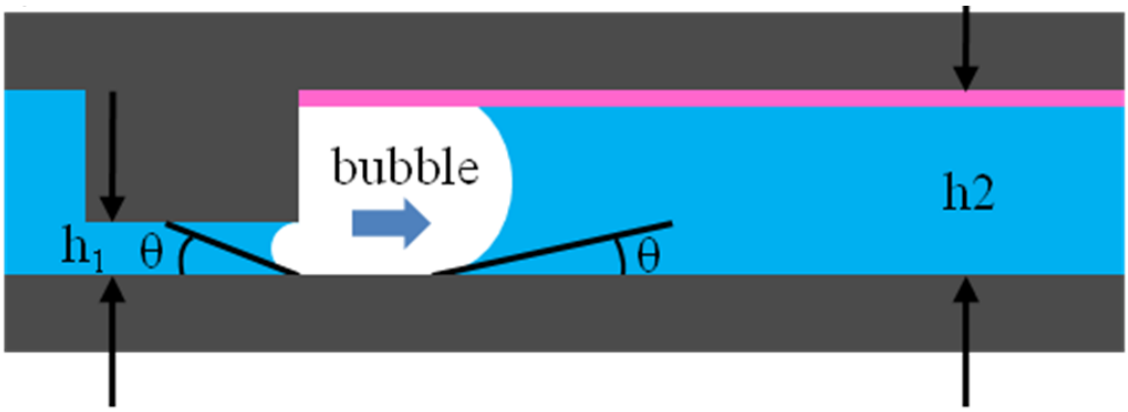

Fig. 1.2. Asymmetric microchannel structures for directional growth and displacement of gas bubbles in liquid.

As is illustrated in Figure 1.2, uneven capillary force and backpressure will be applied to the two meniscuses caused by the asymmetric microchannel dimensional structure. According to Young-Laplace equation, the maximum pressure difference

that the virtual check valve and reaction channel can withstand during the bubble growth is:

$$\Delta P_i^{max} = 2\sigma \left(\frac{1}{h_i} + \frac{1}{w_i} \right) cos\theta \tag{1.3}$$

where σ is the surface tension of liquidgas interface, θ is the receding contact angle of the liquid on the inner surface of the channel, h_i stands for the channel height, w_i stands for the channel width, and $i = 1{,}2$ represents the small virtual check valve channel and the reaction channel, respectively. Because h_1 and w_1 are smaller than h_2 and w_2, ΔP_1^{max} is larger than ΔP_2^{max}. Therefore, if the pressure inside the growing gas bubble (b_1) is between these two values ($\Delta P_1^{max} > P_{bubble} > \Delta P_2^{max}$), the left meniscus will remain at the check valve, while the right meniscus of the growing bubble will move rightward, therefore pushing the flow inside the reaction channel rightward.

As the reaction continues, the bubbles can merge into a larger one that is pushed rightward, like (b2) in Figure 1.1. When its right meniscus touches the hydrophobic membrane, it will be drawn to the PTFE membrane region, also known as a bubble trap, while its left meniscus is still in the hydrophilic region, as is shown in Figure 1.3.

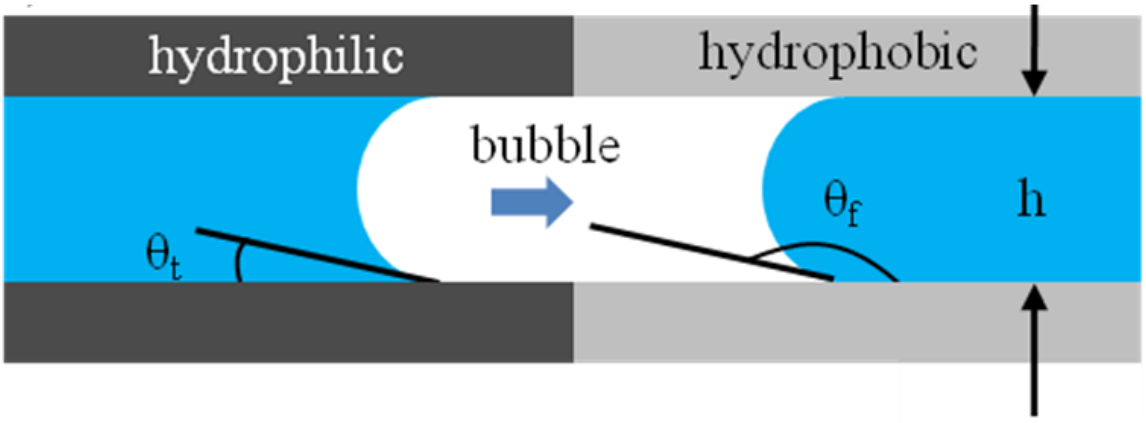

Fig. 1.3. Net capillary force at the hydrophilic and hydrophobic interface (bubble trap).

The contact angle on the surface of the hydrophobic PTFE membrane (θ_f) is larger than 90°, which exerts a capillary pressure to pull the bubble rightwards. At the same time, the contact angle on the surface of the hydrophilic channel wall (θ_t) is smaller than 90°, which exert a capillary pressure to push the bubble rightwards too. Therefore, the bubble would move rightward and pump the liquid from the left fuel reservoir together with it. According to Young-Laplace equation, the total rightward capillary pressure applied upon the gas bubble is:

$$\Delta P_j = -2\sigma \left(\frac{1}{h} + \frac{1}{w}\right) (cos\theta_f - cos\theta_t) \tag{1.4}$$

where r is the surface tension of liquidgas interface, h represents the channel height, and w represents the channel width. Along with the virtual channel neck, this hydrophilichydrophobic junction induces the directional displacement of the bubbles in the system.

When the gas bubble is trapped in the hydrophobic area, like (b3) in Figure 1.1, it will be vented out through the nanoporous membrane due to pressure difference. However, the liquid reactant cannot go through the membrane due to high capillary pressure in the nano-sized pores (200 nm). According to Young-Laplace equation, the maximum pressure for the membrane to hold the liquid without leakage is:

$$P_{leak} = (\Delta P)_{max} = \frac{2\sigma}{r} cos\,(180^\circ - \alpha_{max}) \tag{1.5}$$

If the pressure inside the reaction channel is smaller than the leakage pressure, which is usually the case, only gas can be vented out through the hydrophobic membrane.

When gas bubble (b3) is removed, the surrounding liquid will fill in the vacancy. Therefore a circulation inside the microfluidic channel is achieved. In this way, fresh reactant will constantly move into the reaction channel for a new round of catalytic reaction to keep the gas generation going on.

When the gas venting valve is closed, or the external gas consumption demand is decreased, the gas pressure will keep building up inside the reaction channel, and the gas bubble would eventually fill the whole channel. The contact between the reactant

and the Pt catalyst is therefore cut off, resulting in a self-regulation that stops the reaction, as is illustrated in Figure 1.4. This self-regulating shut down can be restored by simply reopening the gas venting valve or increasing the external gas consumption demand. The pressure inside the reaction channel will be released, thus allowing the reactant solution to contact the catalyst for the self-circulating reaction.

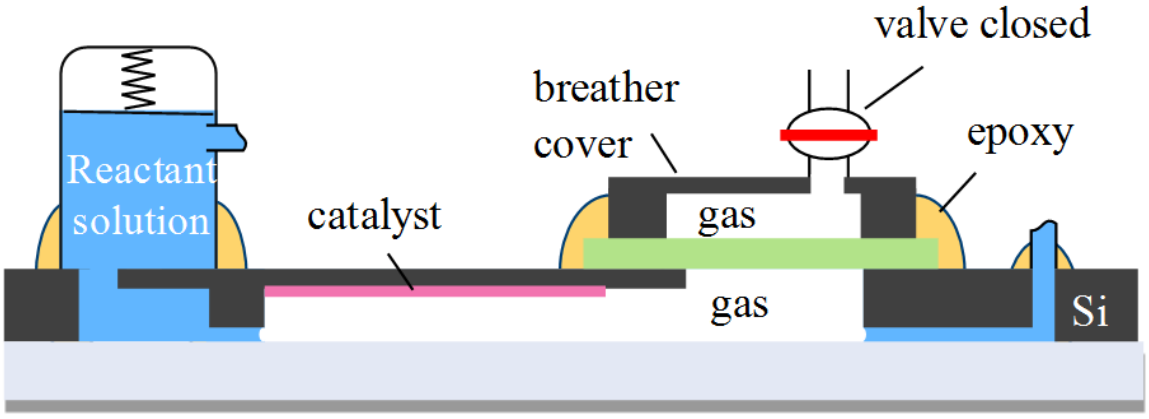

Fig. 1.4. Self-regulation shut down.

1.3 Problem Statement

In the above study, it has been observed that bubbles trapped in the check valve could restrict reactant flow and prematurely shut down the reaction, as is shown in Figure 1.5. Therefore, the objective of the first task is to investigate the effect of blocked virtual check valve by small gas bubbles trapped inside. Our preliminary results in Figure 1.5 have shown that small bubbles occupied many of the V-shaped check valve channels after the self-circulation experiment stopped. It is likely that small bubbles were pushed into the check valve channels during the gas generation reaction and got trapped there. Once all the check-valve channels were blocked, the flow resistance would be significantly increased, leading to premature termination of the reaction and a relatively low utilization rate. This phenomenon can be explained

by the contact angle hysteresis that is defined as the difference between advancing and receding contact angles. If a gas bubble is trapped in the check valve channel, a net pressure difference will be established and it behaves like a back pressure for this gas bubble pump. The self-pumping mechanism cannot pump liquid reactant into the reaction microchannel and the reaction is terminated if the pressure difference is higher than the maximum back pressure that the bubble pump can withstand. The bubbles in the check valve serve as a sybolic problem for the system, because the self-pumping gas generation system is very sensitive to internal pressure, and the channel dimension in such device is very suspectible to bubble block. Therefore, better device design alone with method control are needed to avoid such kind of premature stop.

The dimensions of microchannel will determine the backpressure and the capillary force to pump the reactant solution. Which means the performance of such self-circulating self-regulating microfluidic gas generator is determined by its channel dimension. Therefore, the second proposed task is to seek optimal channel dimension to improve the device performance. There are, however, many changeable parameters in the reaction channel, such as the dimension of the check valves, height and length of the reaction channel, the location of the Pt catalyst and nanoporous membrane, etc. There are infinite amount of combinations from all those parameters, therefore, it's impractical to conduct a thorough study about the optimal channel dimension. However, through carefully designed experiments, the effect of certain parameter can be evaluated, which makes it possible to come up with a good performing microchannel dimension.

1.4 About This Thesis

As is stated above, the purpose of this thesis is to use experimental method to improve the performance of the device by finding the optimal dimensions for the channel structure design. In order to do that, a microfluidic device fabrication method that is time and cost efficient with good resolution is needed. Therefore, the next part

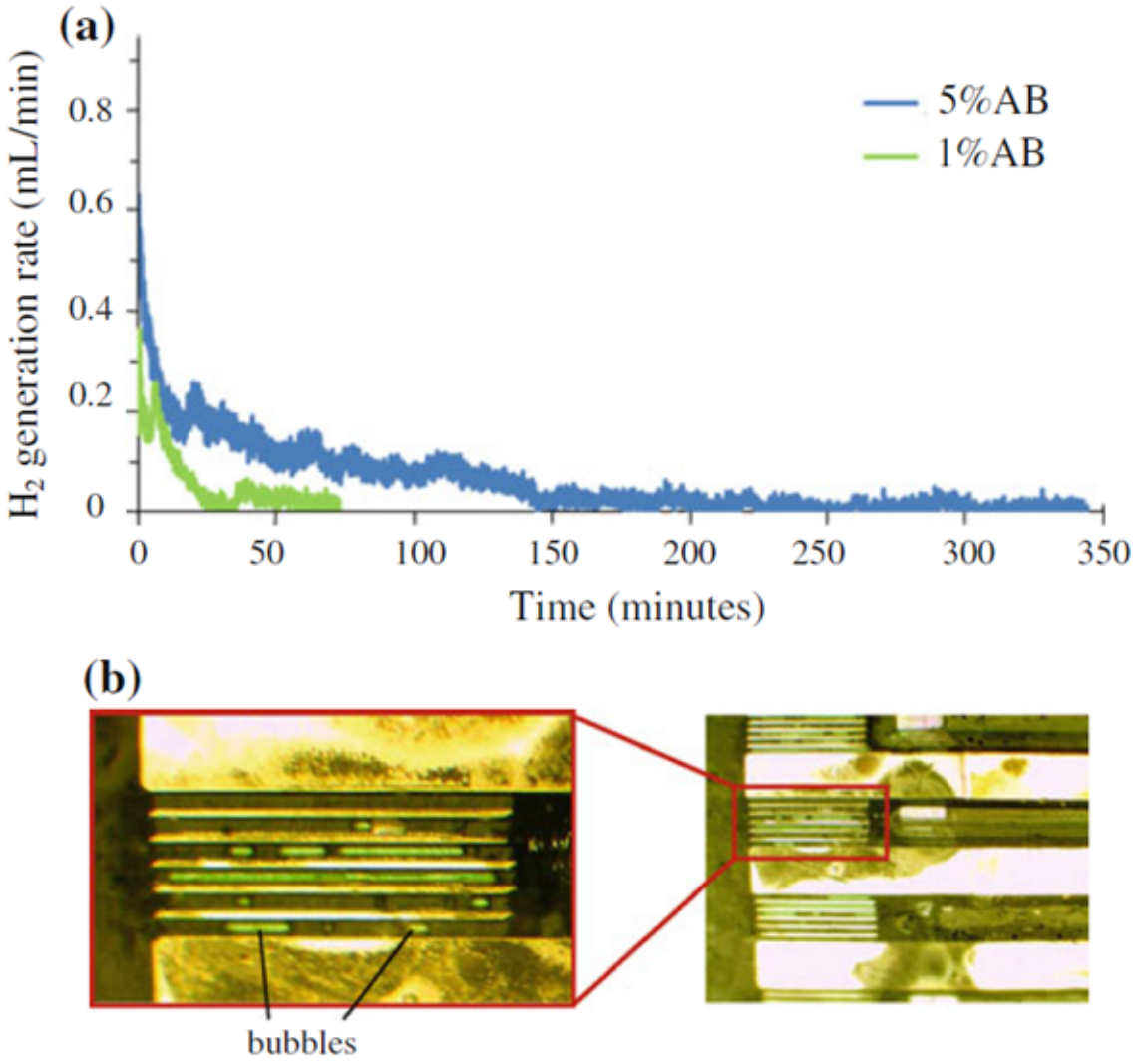

Fig. 1.5. Hydrogen generation profile of 1 percent and 5 percent NH_3BH_3 (AB) (a), and snapshots of virtual check valves. Bubble intrusion in V-shaped channels (b) is thought to restrict reactant flow and prematurely terminate the reaction.

of this thesis will be focusing on the microfabrication method development, which is the major part that composes this thesis. There are two microfabrication methods that have been developed, including the previous double-sided tape-based method, and the more advanced polystyrene film-based method.

Next, the thesis will demonstrate a large amount of carefully designed experiments about the microchannel dimensional test. The testing devices were fabricated using the PS-based method. Based on the collected gas generation rate data, the testing devices with different channel dimensional parameters will be evaluated. In this way, an optimized microfluidic channel dimension under certain preliminary settings has been found.

After that, this thesis will illustrate the study of bubble dynamics using the high speed X-ray imaging facility at APS, Argonne National Laboratory. Ultrafast phase contrast images were captured during the catalytic reaction inside the microchannel. These image data helped us to establish a fundamental understanding about the working mechanism of the self-circulating microfluidic gas generator, which in turn contributed in the optimal channel dimension test.

The thesis then comes into a final conclusion, which is followed by a short list of recommendation for future work on this study.

2. MICROFABRICATION METHOD DEVELOPMENT

This part of thesis will concentrate on the development of microfabrication method that was used for making microfluidic devices for the experiments. There are two methods developed and used in our study, the double-sided tape-based method and the polystyrene film based method. The first method will be illustrated mainly using a conference proceeding, MicroTAS 2014, Oct 26th-30th, San Antonio, TX. While the second more advanced PS-based method will be elaborated by a published journal paper.

2.1 Double-sided Tape and Polymer Film Based Microfabrication Method

In this part, we will illustrate the double-sided tape-based microfabrication method by using a published conference proceeding: Yuanzhi Cao, Likun Zhu, et al., Development of a microfluidic gas generator from an efficient film-based microfabrication method. MicroTAS 2014, October 26-30, San Antonio, Texas.

2.1.1 Preface

We report the development of a microfluidic gas generator using polymer film-based microfabrication method. The method is time and cost efficient and capable of fabricating microfluidic devices with feature resolution lower than 100 μm. Complicated 3-dimentional devices can be fabricated by aligning and stacking multiple layers of patterned polymer (PS, polycarbonate) films and double-sided tapes which are obtained from a digital craft cutter. Integrated with functional features like Pt catalyst, the device can generate a variety of gas (O_2, H_2, etc) through controllable catalytic reaction.

2.1.2 Introduction

Recently, tape and film-based microfabrication method has been studied for rapid prototyping of microfluidic devices due to its low cost and ease of fabrication [14]. But most of the reported film-based microfluidic devices are simple single-layer patterned 2-dimentional (2D) designs, which have limited potential applications. In this paper, we present the design, fabrication and testing results of a 3-dimentional (3D) microfluidic gas generator prototype. This gas generator is used as an example to introduce our new approach of film-based microfabrication method towards lab-use microfluidic research, which usually requires constant change of design and prefers low fabrication cost and short fabrication period. The prototype is a film-based comprehensive microfluidic gas generator that integrates self-circulation, self-regulation, catalytic reaction, and gas/liquid separation. Time and cost efficiency are the biggest merit of this method. The only required facility during the whole process is a digital craft-cutter.

2.1.3 Theory

The working principle of the device is illustrated in Figure 2.1 briefly, when reactant solution comes into contact with the catalyst, the generated gas bubble (b1) will be pushed rightward due to the check valve, thus pushing everything in the reaction channel rightward. When the bubble (b2) reaches the hydrophobic porous membrane, it will be dragged rightward due to hydrophilicity difference and be vented out (b3) and collected. Therefore, self-circulation in the device is achieved and new reactant solution will be pumped into the reaction channel to react until the valve is closed which will cause a self-regulation. The film-based prototype is an alternate version of the silicon-based self-circulating self-regulating gas generator developed by Zhu and Meng.

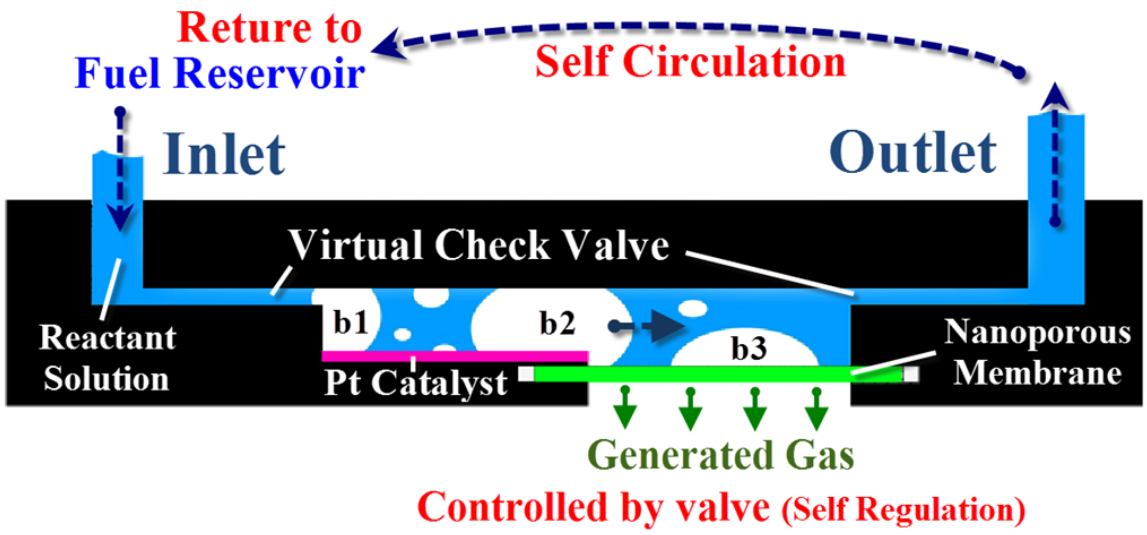

Fig. 2.1. Schematic of the device working principle.

2.1.4 Experimental

Figure 2.2 shows the schematic of the tape-based prototype. It consists of 15 layers of films, tapes, glass slide, tubing connectors, and cube support. The 3D structure was made from both the pattern and the thickness of the layer material, as shown in Figure 2.3. The prototype device was obtained by sequentially aligning and stacking multiple layers of patterned films and double-sided Kapton tape, as shown in Figure 2.4. The patterns were obtained by a digital craft-cutter (Graphtec FC2250, Graphtec America, Irvine, CA) from CAD drawings. Besides, functional features can be easily added into the device. For instance, Pt-black was partially sprayed on the tape layer for catalytic reaction using a shadow mask, and nanoporous membrane was cut in the desired shape and stack-placed in position as the gas/liquid separator. The self-circulating and self-regulating functions were achieved by capillary force difference in different channels. As shown in Figure 2.3, it can be achieved by fabricating different channel depths and treating the surface of certain channel into hydrophilic and leaving

others hydrophobic. The treatment for polystyrene (PS) film was achieved by spraying Lotus Leaf hydrophilic coating or using oxygen plasma machine [15].

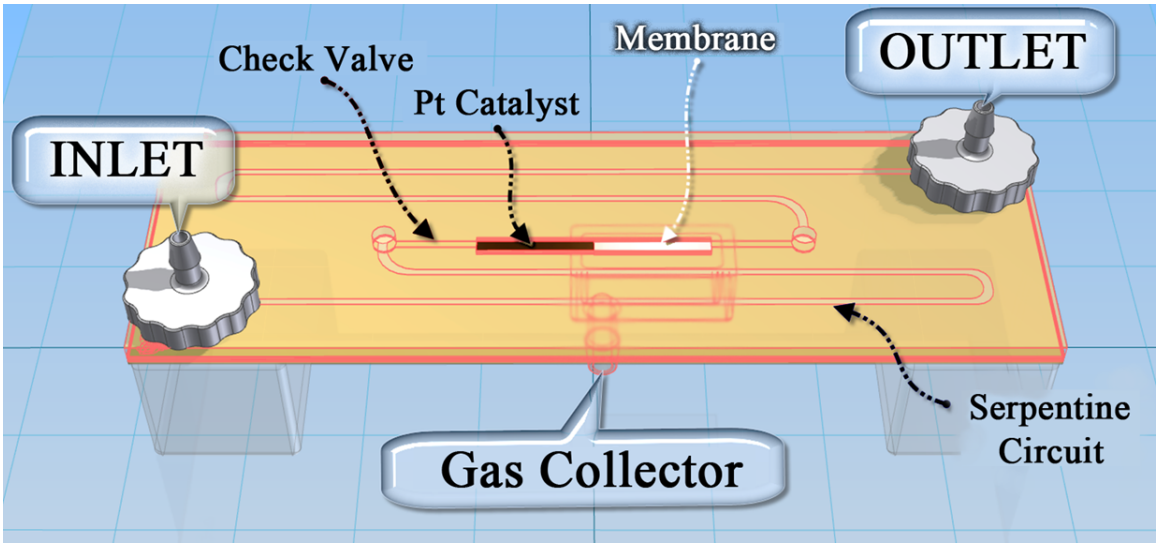

Fig. 2.2. Schematic of film-based microfluidic gas generator. The device is made by aligning and stacking multiple layers of patterned films and tapes, thus 3D structured channels are achieved. The serpentine circuit on the top layer is specially designed to visually measure the self-pumping rate of this single-channel gas generator.

2.1.5 Results and Discussion

The fabricated device was tested with H_2O_2 solutions (for O_2) and NH_3BH_3 solutions (for H_2) at different concentrations. A pressure difference (1 psi) was applied across the gas/liquid separation membrane to provide better venting. The generated gas flow rate was measured by a gas flow meter, and liquid pumping rate measured by monitoring the movement of a liquid/gas meniscus. The gas generation profiles are shown in Figure 2.5 and the summarized characteristics is given in Table 2.1. Figure 2.5 shows that higher reactant concentration caused higher gas generation rate. The fluctuation of gas generation rate is due to the pulsatile pumping of this self-pumping

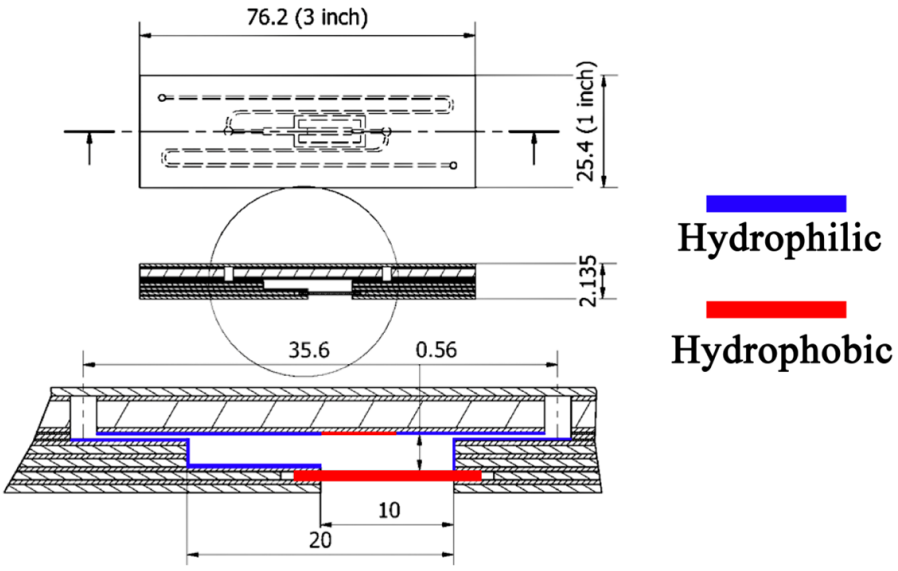

Fig. 2.3. Sectional schematic of the device.

mechanism. It is expected that designs with multiple parallel channels can make the gas generation profile smooth due to the interactions among the channels. Figure 2.6 shows a series of snapshots, each at 0.5 s time intervals, which records the self-pumping gas generation process in the microchannel. The newly generated bubble (b1) expands and pushes b2 rightward, and at the same time, b3 is vented out which creates a rightward dragging force. This provides additional rightward pumping force which keeps the process going repeatedly.

2.1.6 Conclusion

We have successfully demonstrated a microfluidic device fabrication method with the self-circulating self-regulating gas generator as an example. The method shows great potential for scientific research because it provides researchers with a fast and inexpensive testing solution in the area of microfluidics. However, this fabrication method does suffer from low device resolution due to the need for manual assembly during the process.

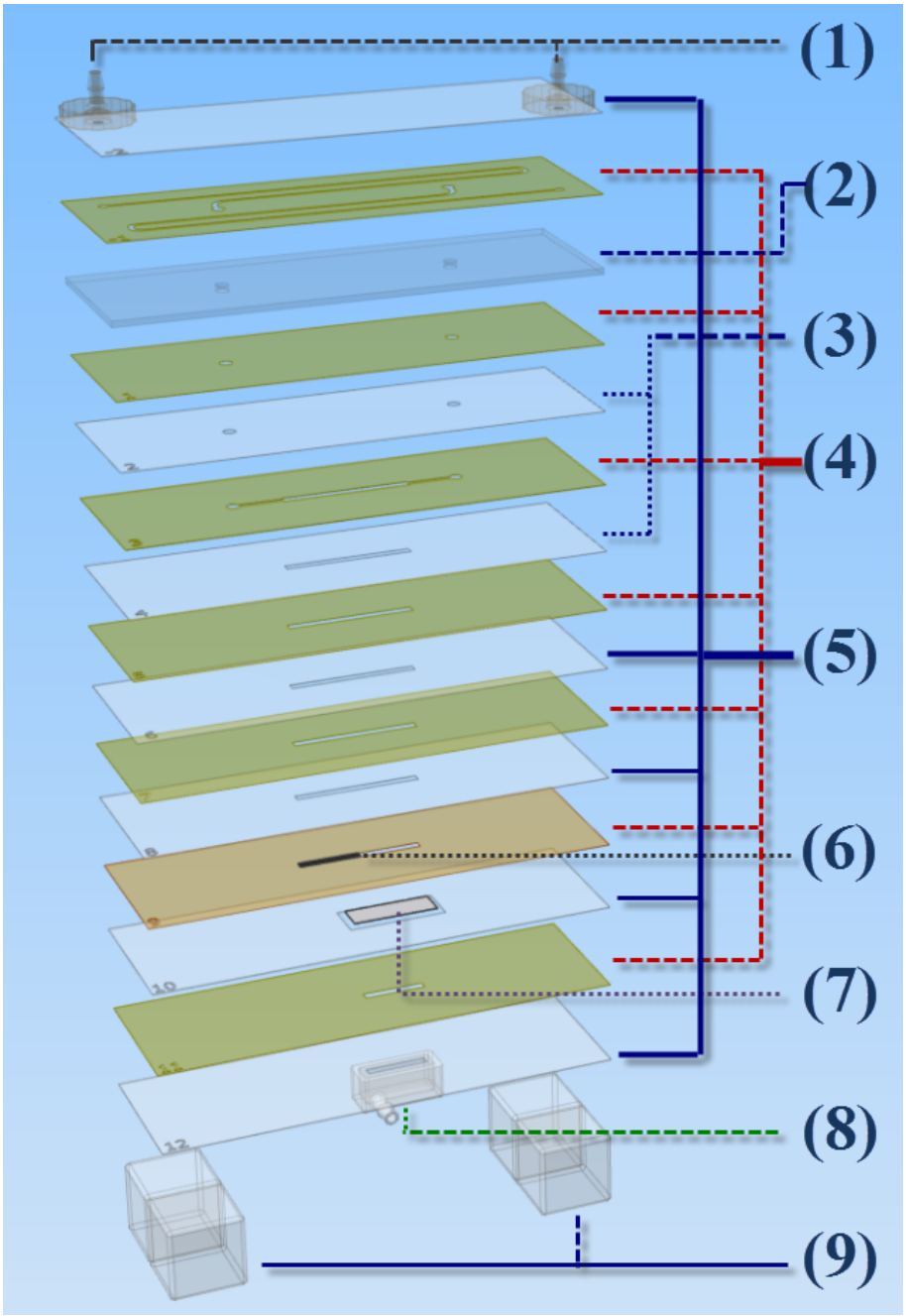

Fig. 2.4. BOM view of the design. (1) Tubing connector for inlet and outlet. (2) Glass slide with two drilled holes. (3) PS film (50 μm). (4) Double-sided tape (70 μm). (5) PS film (125 μm). (6) Pt-black catalyst. (7) Nanoporous hydrophobic membrane for gas/liquid separation. (8) Gas collector. (9) Tube supporting.

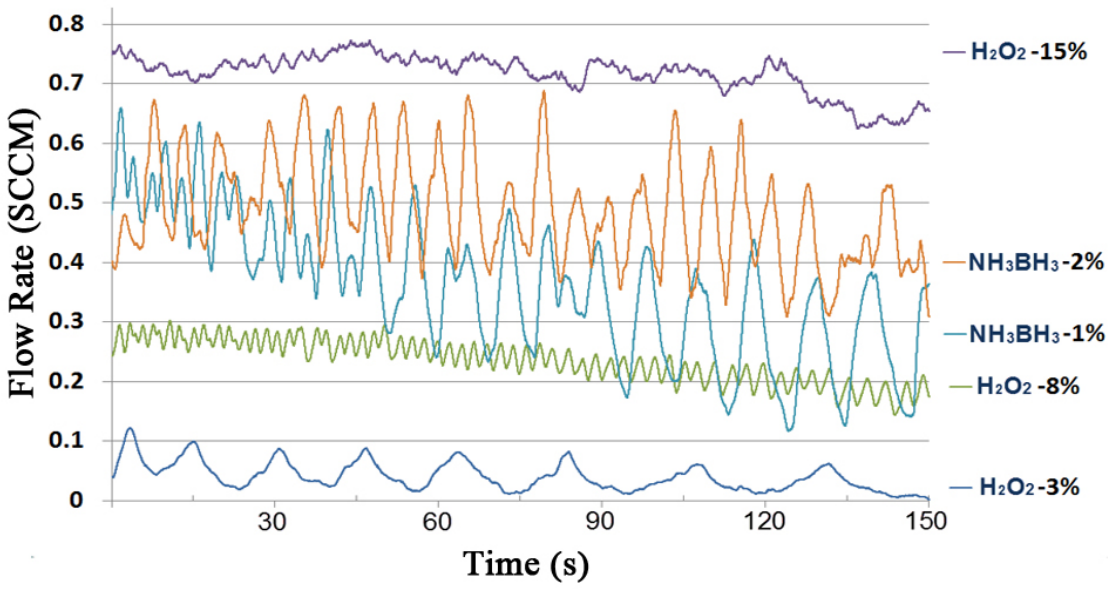

Fig. 2.5. Gas generation profiles for different reactants.

Table 2.1
Gas generation characteristics of the device

Generated gas type	Reactant solution concentration (wt%)	Average gas generation rate in the first 150s (SCCM)	Liquid self pumping rate (uL/s)
O_2 (From H_2O_2)	3	0.038	0.075
	8	0.235	0.348
	15	0.720	0.819
H_2 (From NH_3BH_3)	1	0.361	0.512
	2	0.491	0.602
	4	0.525	0.623

2.2 Polystyrene Film Based Microfabrication Method

In this part, we will present the PS film based microfabrication method by using a journal paper that is published by the Journal of Micromechanics and Microengineering: Yuanzhi Cao, Jacob Bontrager-Singer, Likun Zhu., A 3D microfluidic device

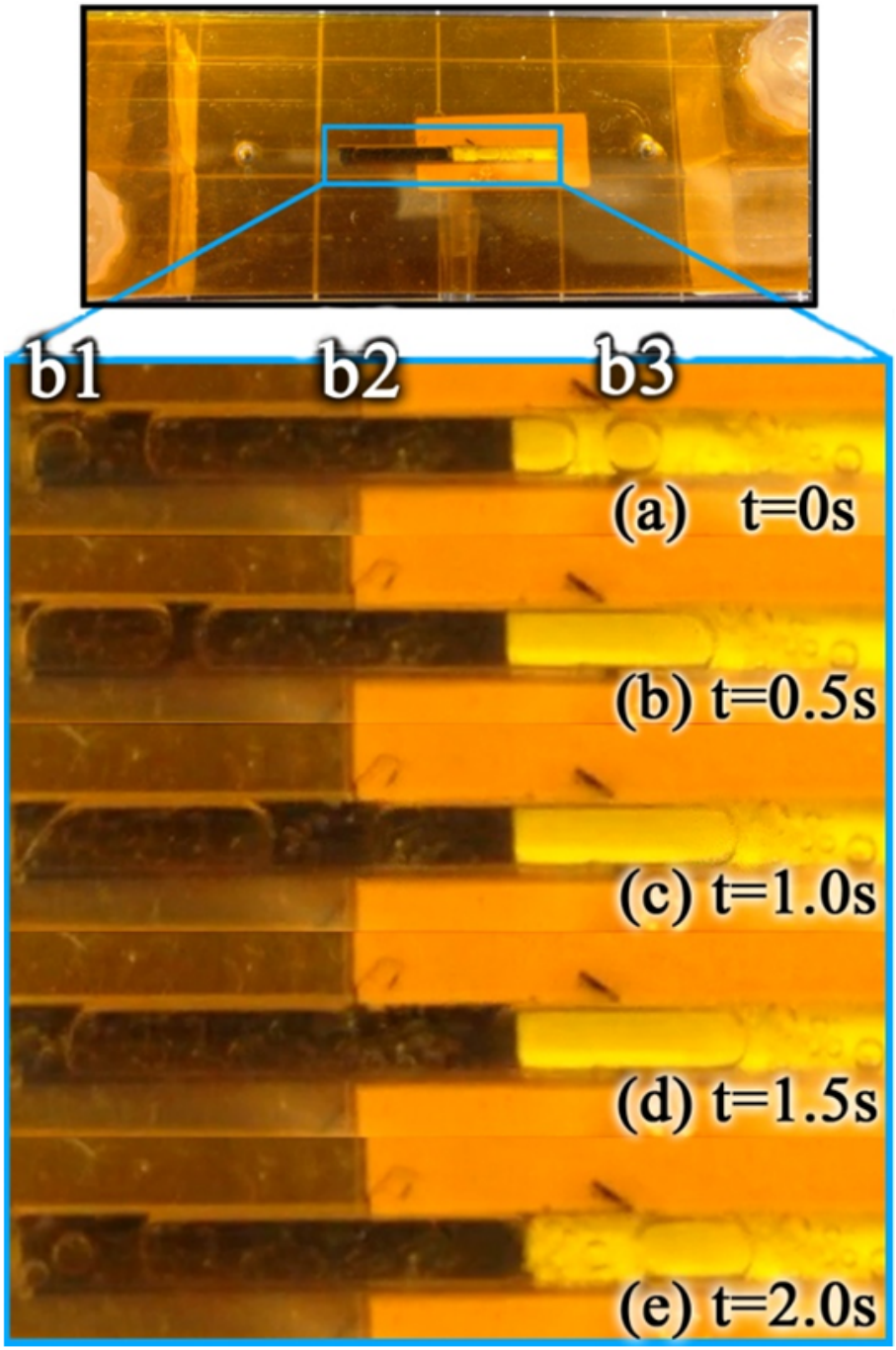

Fig. 2.6. A series of photographs showing gas generation process in the microchannel.

fabrication method using thermopress bonding with multiple layers of polystyrene film.

2.2.1 Preface

In this paper, we present a fabrication method that is capable of making three dimensional (3D) microfluidic devices with multiple layers of homogeneous PS film. PS film is chosen as primary device material due to its advantageous features for microfluidics applications. Thermopress is used as bonding method because it provides sufficient bonding strength while requires no heterogeneous bonding materials. By aligning and sequentially stacking multiple layers (3 to 20) of patterned PS films which are achieved by a craft cutter, complicated 3D structured microfluidic devices can be fabricated by multiple steps of thermopress bonding. The smallest feature can be achieved in this method is around 100 μm, which is limited by the resolution of the cutter (25 μm) as well as the thickness of the PS films. Bonding characteristics of PS films are given in this paper, including PS film bonding strength test, bonding precision assessment, and PS surface wettability manipulation. To demonstrate the capability of this method, the design, fabrication and testing results of a 3D interacting L-shaped passive mixer are presented in the paper.

2.2.2 Introduction

Microfluidics is emerging as a promising direction in chemical and biological applications. In the past decade, lots of research work has been done in the related areas [16–23]. Some of the previous microfluidic devices were based on sophisticated fabrication processes, including photolithography technology on silicon substrates [24], hot embossing and injection molding on polymer materials [25], soft lithography using Poly(dmethylsiloxane) (PDMS) casting [26], and direct machining using CNC milling machine [27]. These fabrication methods were generally capable of achieving high quality devices, yet they also required expensive equipment and long fabrication period.

As for scientific lab researchers who need to constantly adjust their designs, a microfluidic device fabrication method that is time and cost efficient while capable of

obtaining reasonable precision is preferred. In searching for the answer to the above question, one of the solutions led to the emergence of film-based polymer microfluidic devices. In the publication of Yuen et al., they have described the fabrication process using a desktop digital craft cutter to create multiple patterned layers of polymer films. The patterned layers were then assembled and bonded together into a 3D microfluidic device by double-sided pressure sensitive adhesive (PSA) tapes [28]. This method was easy to implement and can reach a feature resolution as high as 200 μm. However, the use of PSA tapes in the device bonding process became a major problem for the method, because it created a non-uniform channel side wall property. In addition, the PSA surface was hydrophobic and it was not desired in microfluidics applications.

In order to fabricate devices with uniform channel surface property, the use of homogeneous film materials is highly preferred. To achieve direct bonding between polymer films, thermopress bonding method was used in this study. The thermo bonding method has been used to fabricate microfluidic devices on different polymer substrates, such as Poly(methylmethacrylate) (PMMA), Polycarbonate (PC), Polyimide (PI), Polyethylene (PE), Poly(ethylene terephthalate) (PET), and Polystyrene (PS) [29–32]. Among polymer film materials, PS possesses advantageous features in microfluidics applications, because it is commonly available, highly transparent, biochemically compatible, and it has good material rigidity [33]. Most importantly, its surface wettability can be easily manipulated by oxygen plasma treatment [15, 34]. Despite all these appealing characteristics, however, the thermopress bonding between PS films has rarely been utilized, and not enough attention has been received to push the research further into device applications.

Therefore, the purpose of this paper is to introduce a microfluidic device fabrication method based on uniform PS films using a digital craft cutter and thermopress bonding method. Different from previous publications regarding PS-based microfluidic devices and thermopress bonding, which usually includes other structural materials like silicon, stainless steel, or other polymers, this paper focuses on using only

patterned PS films from a digital craft cutter to form the complete structure of an integrated microfluidic device. This enables the device of being miniaturized and homogeneous while capable of being fabricated with low cost and short period that will fit a variety of applications. It is also noticed that the publication of Chen et al, has demonstrate a PS based microfabrication method for microfluidics area [35]. They used digital cutter to cut grooves on PS films, and bonded them by heating to 160°C The groove channels would become deeper and thinner upon heating, which made very small channel dimension possible. Our method, on the other hand, is more focused on bonding the PS films under the glass transition temperature of PS (95°C), therefore maintaining the integrity of the channel dimension as designed.

In the following parts of the paper, bonding characterization of PS films will be given first, including the thermopress bonding strength test, bonding feature resolution and deformation examination, and PS surface wettability manipulation demonstration. The paper will then introduce our device fabrication method by presenting a 3D L-shaped microfluidic passive mixer as a demonstrating example. The mixer is achieved by sequentially stacking and aligning 14 layers of patterned PS films (125 μm) with multiple steps of thermopress bonding. The detailed information about the device design, fabrication, and testing results will be given.

2.2.3 Experimental

Material Preparation

The essential of this fabrication method is to use hot press to bond multiple layers of patterned PS film (Goodfellow, Coraopolis, PA) into a microfluidic device with internal 3D microchannels. The schematic of the bonding process is illustrated in Figure 2.7. A hydraulic hot press (Carver, Wabash, IN) is used in this bonding process. As shown in Figure 2.7 (a), under the applied pressure and temperature for a certain amount of time, the interface of PS to PS will be bonded together through molecular fusion transfer. To achieve uniform bonding results, two square glass plates

(54 mm 54 mm 6.35 mm, McMaster, Chicago, IL) are used to sandwich the bonded PS layers. Also, it is important to align the patterned layers before bonding. This can be done by designing alignment features on each pattern and use pins to secure the alignment, as shown in Figure 2.7 (b). The patterns of the film were obtained by a digital craft cutter (FC2250-60 VC, Graphtec, Santa Ana, CA) from computer-aided design (CAD) drawings.The internal 3D structured channel is made possible by the layer pattern as well as the film thickness, as shown in Figure 2.7 (c).

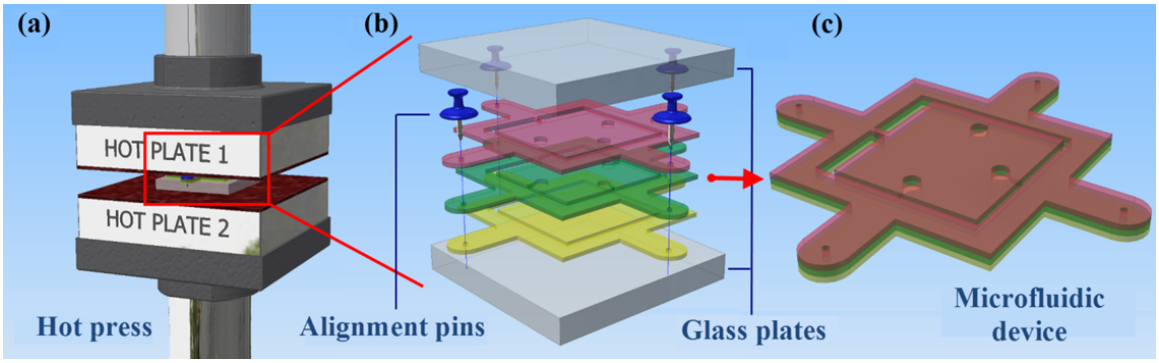

Fig. 2.7. The process overview of PS film-based microfluidic device fabrication method. (a) Thermopress bonding method by a hot press. (b) Patterned PS films sandwiched by glass plates and aligned by pins. (c) Finished film-based device by thermopress bonding.

The thermopress bonding of PS to PS is sensitive to surface cleanness. Contaminations like finger prints, water trace, and fiber dust on the surface will increase the chance of regional bonding defects that will cause critical bonding failure. Therefore, it is important to carefully prepare the surface before bonding. The surface preparation process is as follow: rinse in isopropyl alcohol (IPA) for 1 min and rinse with deionized water (DI) water for 1 min, and another 1 min in IPA, then blow the film dry with air gun. The surface cleaning process should be conducted prior to oxygen plasma treatment. Once the surface is treated, any surface touching should be avoided in case the surface property might be changed.

PS to PS Thermopress Bonding

The thermopress bonding for PS to PS has been studied by several research groups. Our bonding process was based on the work of Young et al. [14]. The hydraulic press was preheated to 93.3°C for 10 min, after which the stack was loaded and the press was closed with 6.9 MPa pressure for 60 min. The heat was then turned off after 30 min to cool down in room temperature while maintaining the pressure for the rest of the time. The bonding was then complete and the PS stack was removed from the press, at which time the stack temperature was around 70°C This gradual release maneuver helped the bonded chip to avoid cracks, which might happen if the chip was still very hot when unloading the bonding force.

PS Thermopress Bonding Strength Test

The bonding strength test was conducted with our specially designed testing devices, as illustrated in Figure 2.8. Air pressure was manually applied to the testing device by a syringe, and the burst pressure of the device was recorded by a pressure sensor (Vernier, Beaverton, OR) to test the tensile pressure of the PS bonding strength. 6 layers of patterned PS film were aligned and bonded to make a testing device by one thermopress bonding. The hollow space has a thickness of 0.5 mm (4 layers of 125 μm thick film), which is large enough to guarantee a uniform pressure distribution. As shown in Figure 2.8 (b), when the pressure was applied from the inlet, the top and bottom bonded layers would resist the device from ballooning until the burst happened. The maximum pressure was recorded and the bonding tensile pressure could be calculated using the following equation:

$$P_{tensile} = \frac{A_1}{A_2} * P_0 \tag{2.1}$$

Where P_0 is the burst pressure monitored by the pressure sensor, A_1 is the inner area where the pressure is applied on, A_2 is the ring-shape bonded area. A_1/A_2 is designed to be 3 so that burst can happen at low pressure.

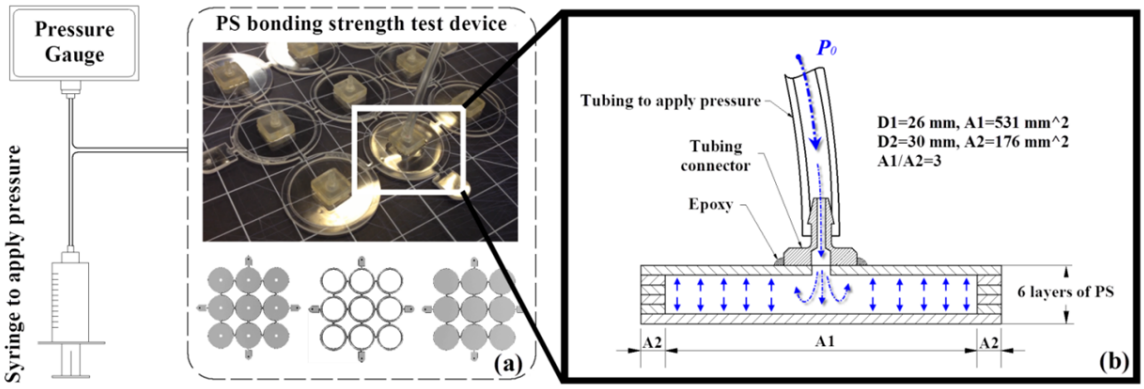

Fig. 2.8. PS thermopress bonding strength test. (a) Bonding strength test process. There are 9 sub-testing devices in one bonded testing device. The inlet pressure was applied from a syringe and measured by a pressure gauge. (b) Testing device schematics. The bonding strength can be characterized by the air pressure monitored to burst the device regarding the related area A1 and A2.

In this study, double cantilever method (also called the crack opening method) was also used to characterize the bonding strength [36]. A thin metal blade (200 μm thick) was inserted between two bonded PS films (125 μm thick), resulting in delamination. The bonding strength can be comparatively assessed by measuring the crack length with an optical microscope (AmScope, Irvine, CA). Shorter crack length means higher bonding strength.

The surface wettability of PS can be easily manipulated by oxygen plasma treatment (120 Watt, 2 min), which is a major advantage of the material for microfluidics applications. However, the plasma treatment can significantly affect the thermopress bonding strength because of surface reaction due to the plasma [14]. Moreover, it is noticed during our experiments that washing the PS films using DI water after oxygen plasma treatment can affect the bonding strength. Therefore, the bonding strength tests were conducted with the two methods in several categories concerning oxygen plasma treatment and washing after the treatment.

PS Surface Wettability Manipulation

One of the advantages of PS as microfluidic device material is that its surface wettability can be easily changed from hydrophobic into hydrophilic by oxygen plasma treatment (120 watt, Plasma Etch PE-50, Carson City, NV), and the hydrophilic surface property can last for months [37]. It is noticed that the surface wettability of PS film after plasma treatment is affected by the treatment time, as well as whether the substrate is washed by DI water after the treatment. Therefore a hydrophilicity test was conducted on PS films to study the wettability effect with different oxygen plasma treatment scenarios.

If using a shadow mask during the oxygen plasma treatment, patterned hydrophilic surface can be achieved and it can be utilized in microfluidics applications. Figure 2.9 presents a demonstrating example. The structure of the device was a hollow box without any geometric channels. However, the internal surface of the device was partially treated by oxygen plasma with a patterned mask, therefore a hydrophilic pattern was achieved on the inside surface of the hollow box, as is illustrated in Figure 2.9 (b). The shadow mask was a one-side smooth thin film performing as protection layer on the polycarbonate film (McMaster, Chicago, IL). It was applied on the PS film by electrostatic force that was strong enough for cutting and plasma treatment, and could be removed without any residue. The film was attached to the PS surface first and then cut by the digital cutter into a patterned mask, the patterned part of the adhesive mask was then removed to expose the underlying PS film to oxygen plasma treatment.

L-shaped Passive Mixer

One of the basic applications of microfluidic device is to mix two or more reagents into one uniform solution. This can be difficult to achieve in a passive manner because the flow in microchannels is usually laminar flow which won't mix fast enough. In order to get the reagents from different inlets to mix uniformly and quickly, complicated

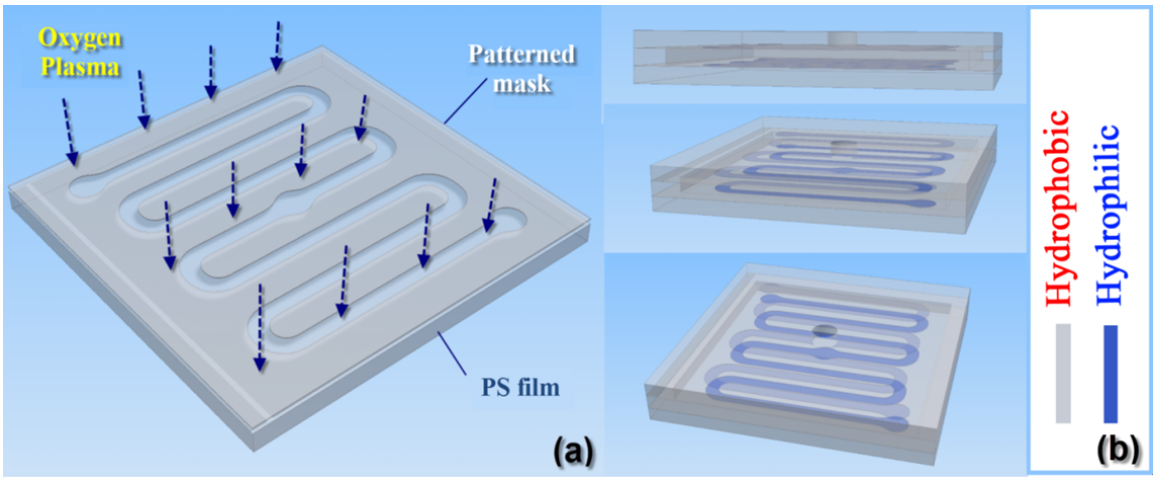

Fig. 2.9. PS surface wettability manipulation by oxygen plasma. (a) Partial oxygen plasma treatment achieved by a shadow mask. (b) Demonstration device with inside hydrophilic pattern.

3D passive mixers can be implemented to achieve better mixing performance [38]. However, it is difficult to fabricate 3D microfluidic mixers compared to the 2D designs. In this study, a 3D L-shaped microfluidic mixer was used to demonstrate the capability of our microfluidic device fabrication method.

The design of the L-shaped passive mixer is shown in Figure 2.10. It is made of 14 layers of 125 μm PS films and it has 3D connected out-of-plane L-shaped channels from sequentially stacking and aligning all the patterned films. To form the internal 3D L-shaped channel demonstrated in Figure 2.10, 14 layers of 125 μm PS films were used, where the first and last film performed as the top and bottom layer of the device. For the rest of the PS films, 4 layers with the same pattern together formed the top part of the 3D channel, followed by 4 layers that formed the middle part of the channel, and another 4 layers with the same pattern that formed the bottom part (please refer to Figure 2.11 for better understanding). Each 4-layer part had channel thickness of 0.5 mm, and the 3D geometry was achieved by both the pattern and the

thickness of the PS films. The design process was completed in CAD software, and the pattern of each layer was transformed to 2D file format for the digital craft cutter.

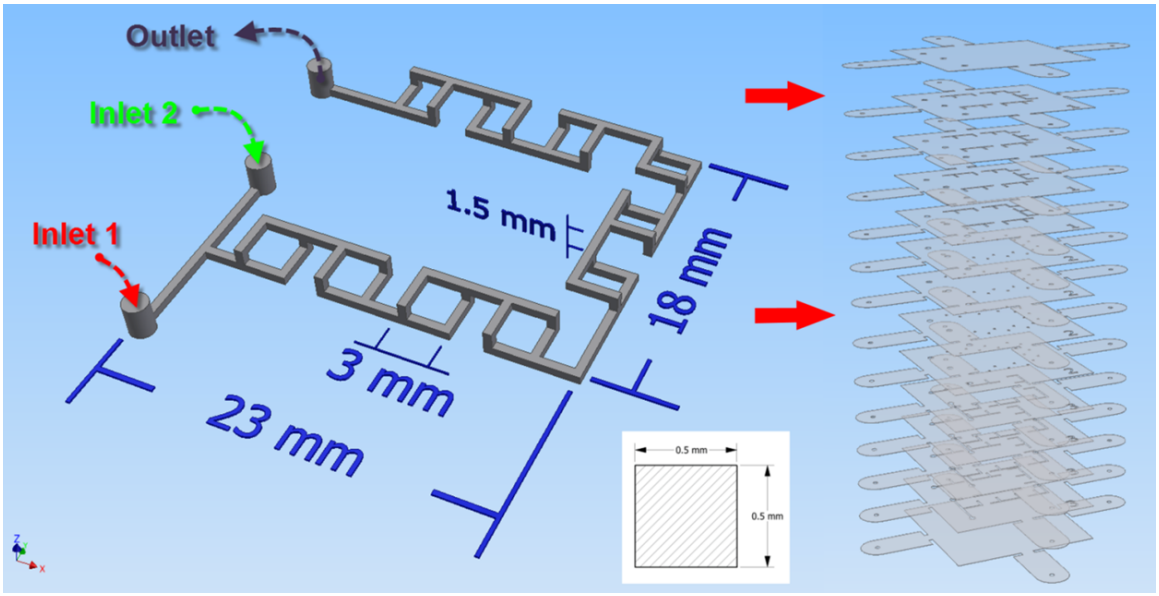

Fig. 2.10. Design schematic of a 3D connected out-of-plane L-shaped passive microfluidic mixer.

After the film pattern was cut and prepared for each layer, the PS films were ready to be bonded together into a device. But for a complicated device with internal 3D channels like this mixer, it cannot be done by simply putting all the films together and complete the device by one thermopress bonding. The reason is that in order to achieve solid thermopress bonding, the bonded structure must not be hollow inside unless no films need to be bonded above or below the hollow feature. Therefore, to achieve solid bonding for the device, multiple steps of bonding were required (3+1), as is illustrated in Figure 2.11 (a). After bonding, the tubing connectors were glued on using epoxy. The finished device is shown in Figure 2.11 (b).

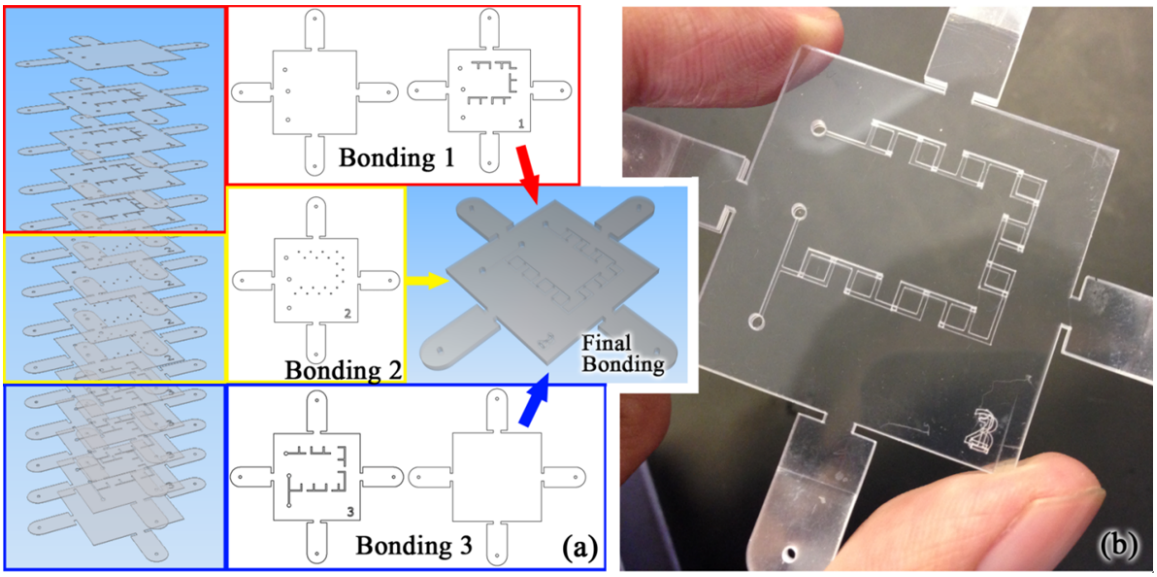

Fig. 2.11. Fabrication process of a 3D microfluidic mixer. (a) L-shaped 3D mixer achieved by multiple steps of thermopress bonding (three sectional bonding and one final bonding to fabricate the device). (b) Fabricated device showcase.

2.2.4 Results and Discussions

PS Bonding Strength Test

The bonding strength test results are summarized in Table 2.2. It is noted that the data in the table is the tensile pressure $P_{tensile}$ converted from P_0 using equation 2.1.The results show that the non-treated samples have the highest bonding strength and the value can reach as high as 375 KPa, while the fully-treated samples have the weakest bonding strength, which is lower than 50 KPa. It is also noted that the test data obtained has a large deviation, especially the non-treated category. This non-uniformity could be caused by the defects on the bonding surface, to which the test is very sensitive due to the burst mechanism. This also explains why the fully treated samples have the smallest deviation, because the oxygen plasma treatment also has surface cleaning effect [31].

Table 2.2
PS bonding strength results summary

Tensile pressure (KPa)	Maxbonding strength	Min bonding strength	Average bonding strength	Standard deviation
Non-treated	375.5	97.5	200.8	27.5
Half-treated	171.5	56.6	96.5	11.4
Fully-treated	87.8	43.5	63.7	4.4

It is shown in Table 2.2 that the weakest bonding case can still reach a bonding strength larger than 40 KPa, which is sufficient for most of the microfluidic devices. Because of the mechanical property of PS, the material after thermopress bonding becomes rigid which is resistive to regional failure like burst deformation. It will hold the integrity of the whole device before a total device burst failure happens, which requires much more pressure and is less likely to happen. Moreover, if stronger bonding strength is required in the device, a shadow mask can be used for the oxygen plasma treatment to protect the bonding surface while exposing the channel surface.

The above test was designed to give quantitative evaluation of PS bonding strength in several basic scenarios, where the PS films were not washed after oxygen plasma treatment. The following double cantilever method test gives a more comprehensive assessment on PS thermopress bonding under a variety of conditions. In the test, a thin blade (200 μm) was inserted between two bonded PS films (125 μm), and the crack length was measured to indicate bonding strength. Each of the tests was conducted on three individual samples to generate more than 20 result data. The results are shown in Table 2.3.

In this study, we used the double cantilever method to provide a comparative assessment for different bonding conditions. The testing results have shown that oxygen plasma treatment can significantly decrease the thermopress bonding strength of PS to PS, and the fully-treated PS samples have the weakest thermopress bonding

Table 2.3
Double cantilever method results summary

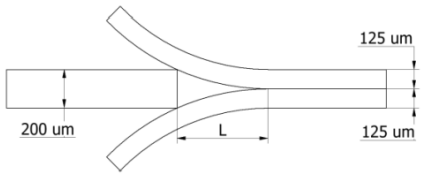	L - Crack length (mm)	Normalized bonding strength	Standard deviation
No plasma treatment	0.475	1	0.033
Half-treated (not washed)	0.798	0.126	0.091
Half-treated (washed)	0.668	0.256	0.090
Fully-treated (both washed)	0.933	0.067	0.085
Fully-treated (non-washed)	1.020	0.047	0.048
Fully-treated (half-washed)	0.993	0.052	0.082

strength. This result shows the same trend with the previous bonding strength test by the chips.

To better understand and explain our results, we have conducted X-ray Photoelectron Spectroscopy (XPS) to study the surface chemical change due to the effect of oxygen plasma treatment. The count per second as in the label of the figure means counts per seconds, as XPS counts electrons ejected from a sample surface when irradiated by x-rays. It is worth mentioning that a direct comparison of peak areas is not a recommended means of comparing samples for the following reasons. An XPS spectrum is a combination of the number of electrons leaving the sample surface and the ability of the instrumentation to record these electrons; not all the electrons emitted from the sample are recorded by the instrument. Further, the efficiency with which emitted electrons are recorded depends on the kinetic energy of the electrons, which in turn depends on the operating mode of the instrument. As a result, the best way to compare XPS intensities is via, so called, percentage atomic concentrations. The key feature of these percentage atomic concentrations is the representation of the

intensities as a percentage, that is, the ratio of the intensity to the total intensity of electrons in the measurement.

Since 2 min was the treatment time we used in our bonding test, two PS samples (washed and not washed after treatment) with such treatment, alone with a reference PS sample without treatment, were tested in the C 1s XPS experiment. Figure 2.12 (a) shows the comparative survey spectrum of the two treated PS samples with the reference untreated PS sample. From the figure, we can notice that the intensity of Pi-Pi bond in the PS sample was decreased after the treatment. This indicates the broken of large polymer molecules into smaller molecules on the surface [34]. The chemical expression of PS is shown in (2.2), it is noticed that PS only has carbon and hydrogen as its composition elements.

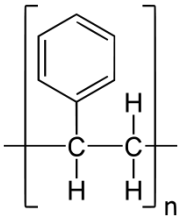

(2.2)

However, due to the oxygen plasma treatment, oxygen element has been added to the chemical composition and new bonds like C-O-C and C=O were introduced to the PS surface, which can also be observed in the Figure 2.12. This explains why bonding strength was significantly reduced for oxygen plasma treated PS films, because the newly introduced surface substances have different material property with polystyrene. Therefore the thermopress bonding temperature at 93.3°C which was designed according to the Tg of PS (95°C), was no longer suitable for the molecular fusion of the newly introduced substances [34]. This caused poor molecular fusion for the treated PS films with current thermopress bonding temperature, which resulted in weak bonding strength, especially for the fully treated case described above.

It is also noticed that whether the films were washed after the plasma treatment can slightly affect the bonding strength, but not enough to make significant difference. Figure 2.12 (b,c) and Table 2.4 have demonstrated data to show the surface chemical

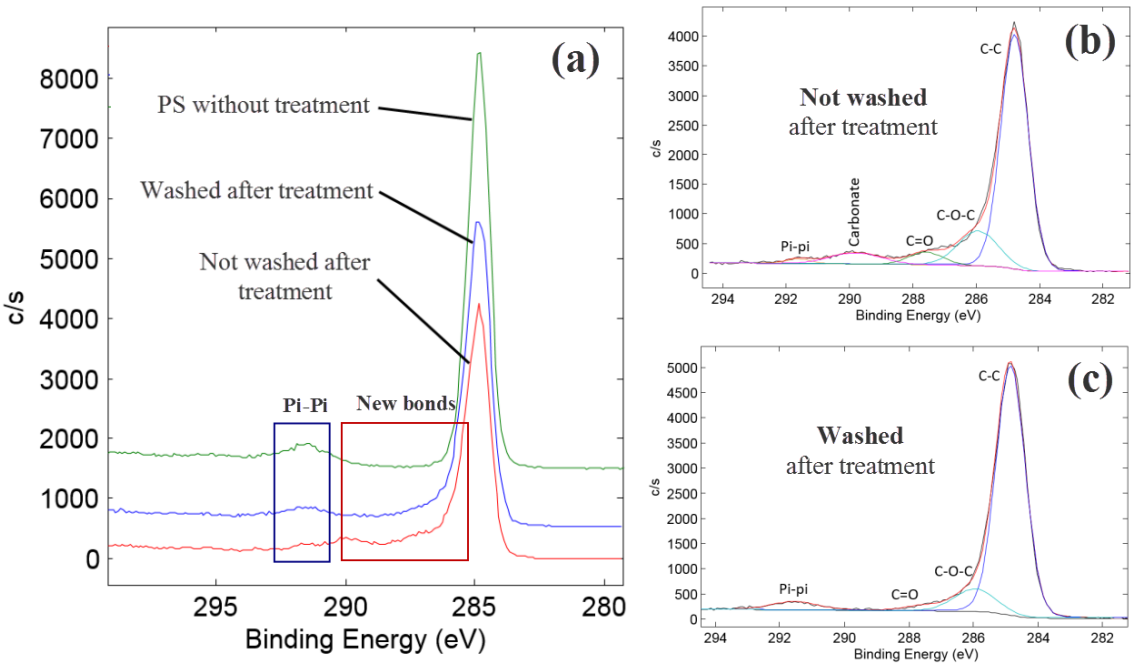

Fig. 2.12. C 1s XPS test on oxygen plasma treated (2 min) PS samples. (a) Comparative survey spectrum with three PS samples. (b,c) Comparison between the washed and not washed PS sample after treatment.

composition for the two treated PS samples, and there is noticeable difference in carbonate, C=O, and C-O-C for the two samples. This is because during the oxygen plasma treatment, large polymer molecules on PS surface were broken into smaller molecules that were still attached to the surface, but could be easily washed away. This layer of broken small molecules on the surface will act like barrier to impede the molecular fusion process during the thermopress bonding, therefore resulting in the fact that washed PS samples have a slightly higher bonding strength than the non-washed ones.

From the comparative data showed in Table 2.4, it is noticed that the carbonate has been completely washed away, which is due to its high solubility. And the Pi-Pi bond intensity has increased after washing, which is because of the wash away

Table 2.4
XPS result summary for PS samples with/without wash after treatment

	Pi-Pi	Carbonate	C=O	C-O-C	C-C
Washed after treatment	4.45%	0%	1.82%	10.94%	82.79%
Not washed after treatment	1.3%	6.41%	4.66%	15.31%	72.32%

of other substances like carbonate, C=O, and C-O-C, that exposed more PS and therefore increased the overall detected percentage of the Pi-Pi bond.

However, this result is different from several previous publications. For instance, Bhattacharyya et al. showed that the fully plasma treated PS substrates have the highest bonding strength [39], and Young et al. showed that the fully-treated PS samples have a stronger bonding strength than the half-treated ones, yet still a lot weaker than the non-treated PS samples [14]. These controversial results on the subject could be due to the different bonding conditions (bonding recipes, facilities, PS material properties, surface treatment, etc.) that were implemented during the experiments by different research groups, which could affect the bonding strength. For instance, Bhattacharyya et al. used PS material from Pria Diagnostics (Menlo Park, CA, USA).Young et al. treated the PS surface at 60 W for 12 sec and the process involves sonication (10 min, 50°C) and incubation (37°C 5 percent CO_2) before bonding.

Bonding Deformation and Channel Resolution

To examine the deformation after the thermopress bonding, new testing devices were designed. The testing device was made of multiple layers of 125 μm thick PS film, with the patterns for measurement. The normal dimension was measured by a vernier caliper, while the transverse dimensions were measure by a microscope (AmScope, Irvine, CA). After the theromopress bonding with conditions mentioned above, the device normal thickness decreased from 1750 μm to 1650 μm (5.7 percent),

while the transverse dimension of a pattern changed from 5000 μm to 4900 μm (2 percent). This means a feature dimension change around 5 percent can happen after thermopress bonding, which will affect the overall resolution of the device. It is noted that if high precision is required, the dimension adjustment should be considered into the design to compensate the deformation.

The following examination is about the channel resolution of the microfluidic devices achieved by this fabrication method. Figure 2.13 shows the SEM images of the cross-section view of the microchannels achieved with our method. A wide channel (125 μm * 700 μm) is shown in Figure 2.13 (a) with very little channel collapse or deformation. This desirable result is attributed to the high stiffness of the pre-bonded top and bottom capping layers of the channel, because thermopress bonding process greatly increases rigidity of the material [29]. Figure 2.13 (b) shows a channel cross-section view with a dimension of 125 μm * 125 μm, which is the resolution for this thickness to come up with decent microchannels. It is believed that with thinner PS films (as low as 25 μm that is commercially available), even higher channel resolution might be achieved.

The resolution of the device is also affected by the alignment tolerance in case of multiple layers bonding, which in turn is decided by the film pattern itself (decided by the digital cutter's tolerance, currently 25 μm) as well as the alignment method. It was examined under SEM that the alignment tolerance of our current method is around 35 μm, which is good enough for regular microfluidic devices whose channel width is about 0.5-1 mm. If higher alignment tolerance is needed for better device resolution, more sophisticated alignment method can be implemented.

PS Surface Wettability Manipulation

A surface wettability test was conducted to study the PS surface wetting with different oxygen plasma treatment time. Figure 2.14 shows the testing result by measuring the contact angle, which is obtained by a goniometer (rame-hart, Succasunna,

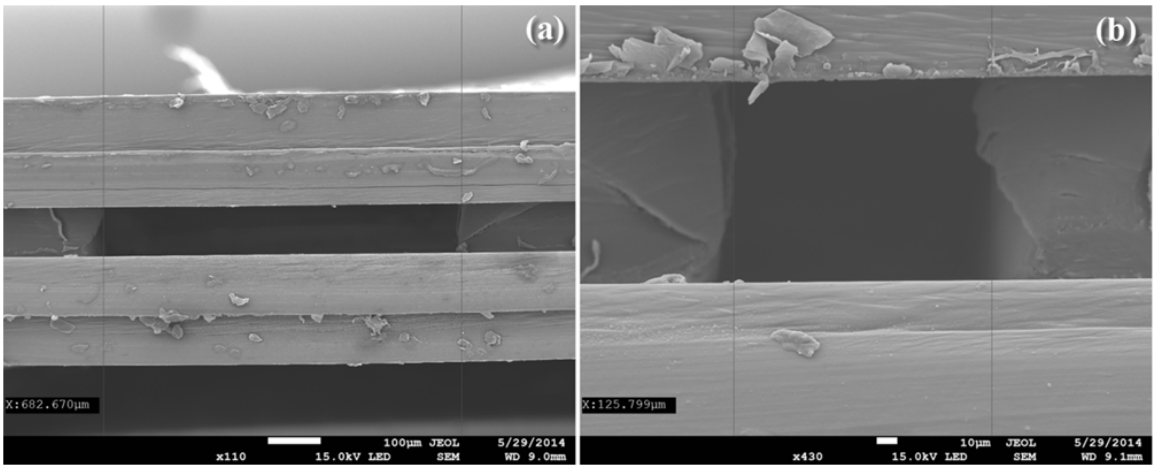

Fig. 2.13. SEM images of channel sectional view for resolution and deformation examination. (a) Channel width is 700 μm, channel height is the thickness of 1 layer of PS film, 125 μm. (b) The smallest microfluidic channel achieved with this method is 125 μm *125 μm.

NJ). As shown in Figure 2.14, the PS films used in the experiment are hydrophobic in nature and have a contact angle of 93°. After the oxygen plasma treatment (120 watt, Plasma Etch PE-50), the measured contact angle decreased dramatically, making the surface hydrophilic. It is noticed that the measured contact angle of the washed samples is a little higher than the non-washed samples, which can be explained by the same reason in the bonding strength test. Generally, longer plasma treatment time results in lower contact angle. The contact angle tends to stabilize after 4 min of treatment. The stabilized contact angle approximates 25 degrees for the washed sample, and 18 degrees for the unwashed sample. This contact angle difference for the two cases can be explained in Table 2.4. The unwashed PS sample has more oxygen containing substance on the surface than the washed PS sample, which is the reason it is more hydrophilic.

Since the surface wettability of PS can be easily manipulated, when using a patterned shadow mask during the oxygen plasma treatment, a patterned hydrophilic surface can be created. The device shown in Figure 2.15 is an example to utilize this

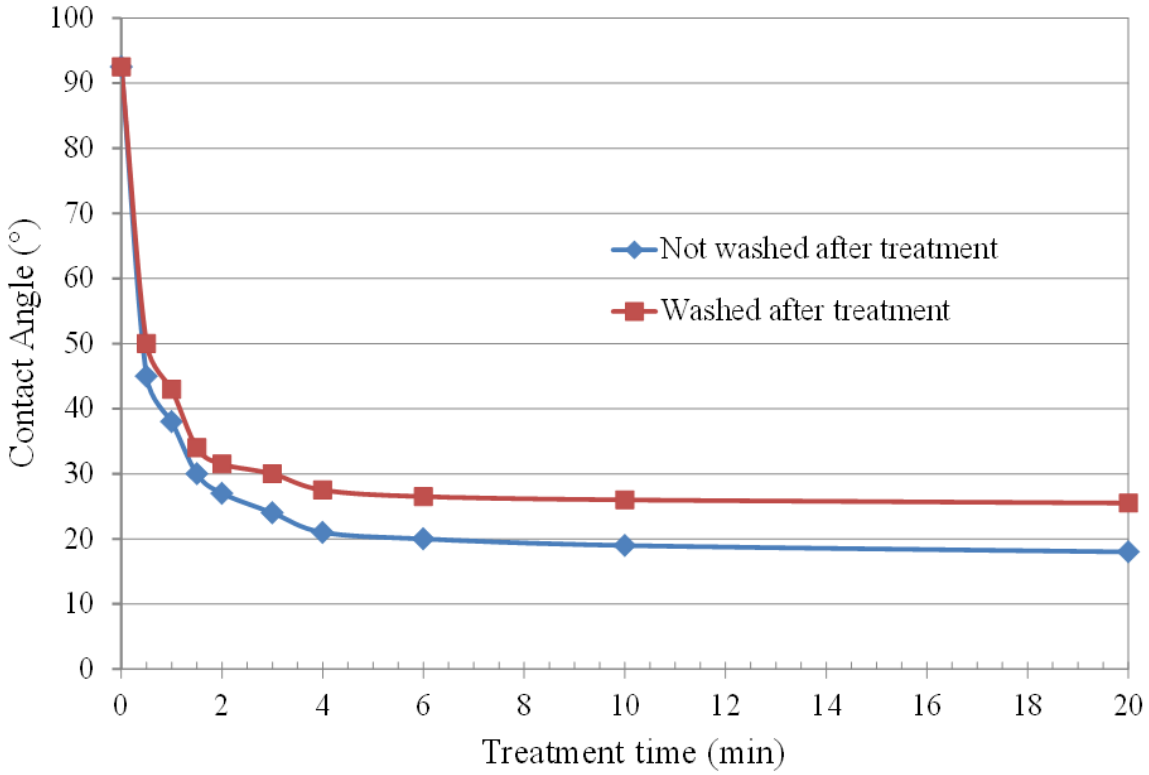

Fig. 2.14. PS surface wettability testing result. Longer treatment time results in smaller contact angle, and the value tends to be stabilized after 4 min of treatment with oxygen plasma (120 watt). It is also noted from the result that washing the samples after plasma treatment can slightly increase the contact angle.

surface manipulation property as is explained in the experimental part. Because of this regional patterned wettability, when the green liquid was pumped from the inlet at a rate of 20 μL/min by a syringe pump (KD Scientific, Holliston, MA), the green solution went through the pattern instead of spreading randomly even though there was no structural channel inside the device.

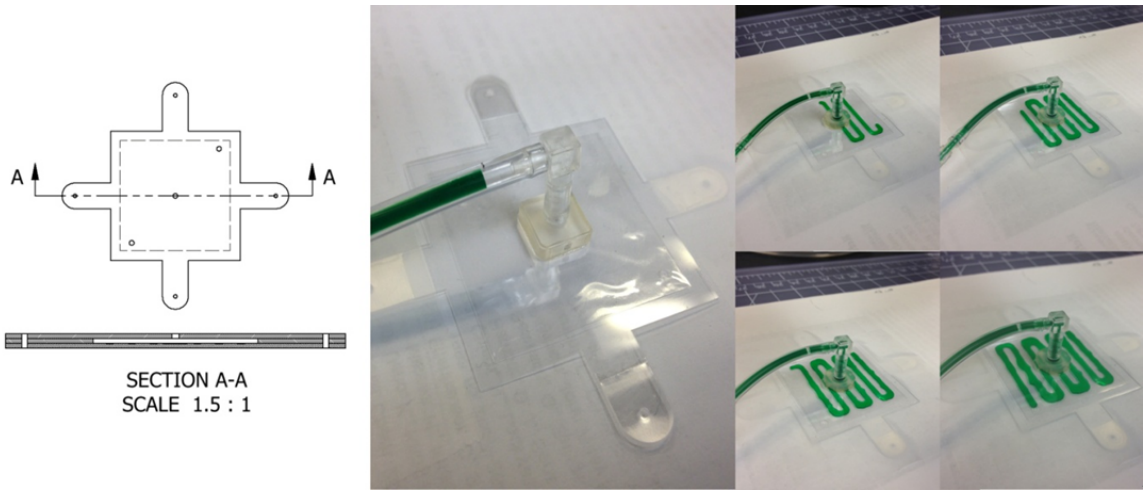

Fig. 2.15. PS surface wettability manipulation demonstration. Since the inside surface of the testing device is partially treated by oxygen plasma to be hydrophilic, the injected green solution travels through the pre-treated hydrophilic pattern even though there is no physical channel in the hollow structure.

L-Shaped 3D Passive Mixer

To test the device, we used a syringe pump to simultaneously pump red and green solutions from the inlet at a flow rate of 50 μL/min. As shown in Figure 2.16, the two different colored solutions were optically observed to be fully mixed at around 20 mm after they entered the device. Given that the sectional area was 0.25 mm^2, and the combined flow rate of the solution was 100 μL/min, which meant it only took 3 s for the solutions to mix in the device once entered. The reason of this good mixing result is explained in Figure 2.16 (f). Because in the 3D microchannel design, the two reagents were split into two streams and forced to join together, and this agitating passive behavior was continuously repeated which greatly promoted mixing effect. If the splitting and joining junctions can be made closer to each other (3 mm in current device), the mixing efficiency can be increased significantly. It is also worth mentioning that the bonding method has very high yield, about 90 percent for single

step two-layer bonding, and almost 100 percent for multiple layers bonding. The occasional bonding failure region only appears at the edge of the bonded chip, where no important features are usually designed. Moreover, the bonding failure region can easily be repaired by repeated bonding during the multiple layers bonding process.

2.2.5 Conclusions

In this paper, we have introduced a device fabrication method for microfluidics applications and conducted a series of experiments to test its validity. The bonding strength tests have shown bonding tensile pressure of the device ranging from 43.5 KPa to 375.5 KPa, which is sufficient for microfluidics applications. The bonding deformation check from the SEM images showed very little channel collapse. PS surface wettability manipulation has shown controllable device surface property, that has significant meaning for microfluidics applications. And finally, the successful test of the 3D L-shaped microfluidic mixer validates our method to fabricate 3D microfluidic devices from PS films. This bonding method has very high yield, about 90 percent for single step two-layer bonding, and almost 100 percent for multiple layers bonding.

The merit of this method is that it provides an inexpensive, fast, and relatively accurate way to fabricate microfluidic devices. The equipment needed during the process are a digital craft cutter and a hydraulic hot press. The primary device material is PS, which is commonly available. Once the design is done, it only takes several hours to fabricate a device, including film material preparation and thermo-press bonding. The feature resolution of this method is limited by both the pattern resolution from the digital craft cutter (25 μm) and the film thickness, which can be found commercially available to be as low as 25 μm. Therefore, we believe that this method is capable of a variety of microfluidics applications, and it is especially helpful to scientific lab researchers who constantly need to change their designs.

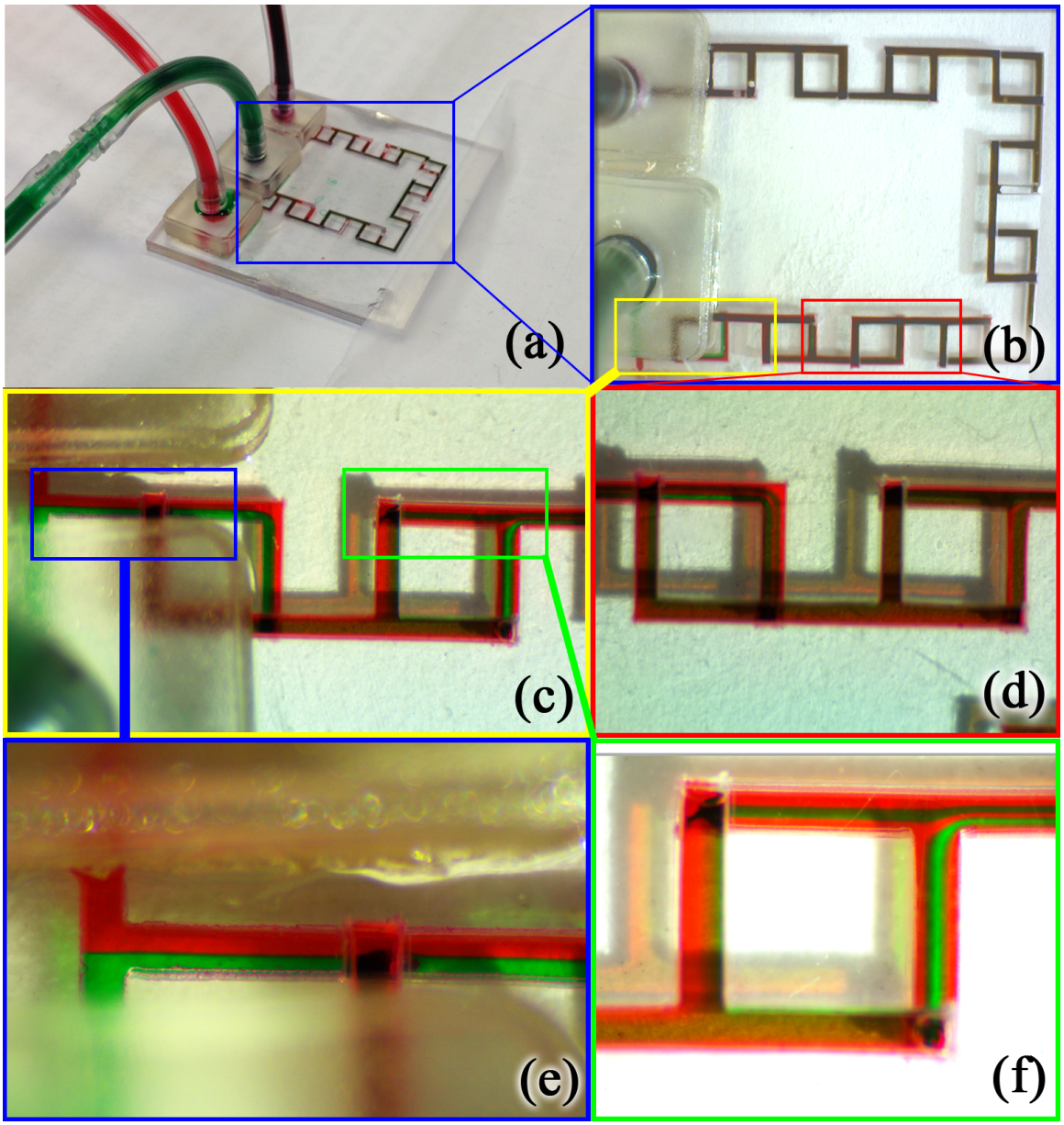

Fig. 2.16. Testing result of the 3D L-shaped microfluidic mixer. (a,b,c) Mixer test demonstration. (d) Two colored reagent mixed uniformly after entering the device in about 10 mm. (e) Laminar flow in the T-shape entrance results in poor mixing. (f) Repeated splitting and emerging the reagents greatly promotes mixing.

2.3 Microfabrication Method Summary

We have so far developed two microfabrication methods for producing microfluidic devices. They are the double-sided tape and polymer film-based method, and the more advanced PS film-based method. Together with the silicon-based lithography method that was used to fabricate the prototype, we now put these three microfabrication methods together and evaluate their pros and cons.

Table 2.5
Comparison summary between three fabrication methods

	Double-sided tape method	Polymer film method	Lithography method
Facility and material requirement	Digital cutter, polymer films, double-sided tapes	Digital cutter, hydraulic press, oxygen plasma machine, polystyrene films	Clean room, reactive ion etching machine, high temperature vacuum furnace, chemical vapor deposition equipment, silicon wafer
Facility and fabrication cost	$10000	$30000	Multi-million
Fabrication time	1 day	Several hours	Several days
Device resolution	300 μm – 500 μm	50 μm – 100 μm	Less than 1 μm
Notes	Requires manual assembly, uses heterogamous bonding material	Uses polystyrene films only	

From the comparison summary between the three microfabrication methods in Table 2.5, we can find that the double-sided tape based method is the most inexpensive fabrication method, but it requires manual assembly, which takes a lot of time and effort, and also results in poor device resolution. Besides, it uses tape as heterogeneous bonding agent, which is hydrophobic and undesirable. The lithography method, on the other hand, uses silicon as basic material and is capable of achieving very high device resolution, however, it requires very expensive facilities and long fabrication period, which is the reason it is also undesirable. Compared to these two

methods, our PS based microfabrication method is capable of achieving device resolution that is good enough for testing purpose. It only needs inexpensive facilities and the fabrication can be completed in a few hours, which is the reason it is the preferred microfabrication method in our research, where design change and new device fabrication are constantly needed.

3. MICROFLUIDIC GAS GENERATOR CHANNEL OPTIMIZATION

In this part of the thesis, we will focus on the study of channel dimension optimization of our proposed microfluidic gas generation system to seek performance improvement. Based on our existing understanding and experiences, we already have some basic ideas about the dimension range for the microfluidic reaction channel. Figure 3.1 gives an illustration about the dimensions in the actual testing microfluidic devices that were fabricated using our previously introduced PS-based thermopress bonding method in Section 2.2.

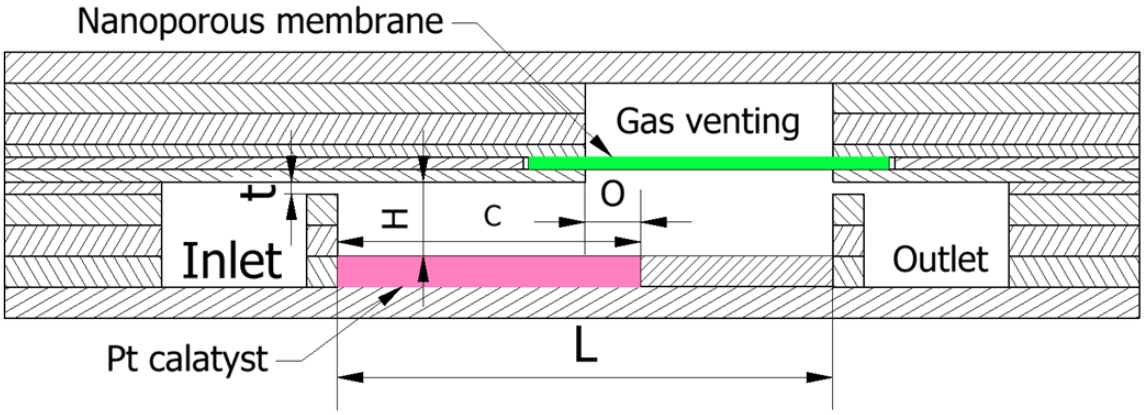

Fig. 3.1. Schematic of the channel dimensions in the microfluidic gas generator.

In the PS-based microchannel, everywhere is treated by oxygen plasma to acquire a hydrophilic surface wetting property, except the hydrophobic nanoporous membrane. This default channel design has two symmetric check valves, whose thickness is a layer of 50 μm PS film. Inside the reaction channel, whose length is L, there are asymmetrically located Pt catalyst and venting membrane, which cause the unidi-

rectional pumping. The catalyst lies from the left side of the reaction channel, with a length of C, while the venting membrane lies from the right side of the reaction channel, with an overlapping length of O with the catalyst. The height of the reaction channel is H, and the width of the channel is T, which is not shown in the figure. The total 3D structure of the channel is a simple extrusion of this 2D drawing in Figure 3.1, without any longitudinal features.

The optimal channel dimension is a combination of all the dimensions mentioned in Figure 3.1, which is not studied in this thesis. However, with the guidance of experimental experiences, we can concentrate on the important ones. To conduct such experiments, we need to fabricate testing devices with different channel dimensions and test them. Then based on the testing results, which is the gas generating performances, we can evaluate the dimensions and find out the optimized channel design.

3.1 Testing Device Design and Fabrication

During the study, we have come up with more than 10 different designs for the dimensional test. Early versions more or less suffered from design and fabrication flaws that were unable to provide satisfactory results. Through this trial and error process, we have been constantly improving our design, and eventually achieved the proper results. This part of the thesis is going to use one of our eligible testing devices as an example to illustrate the device design and fabrication process.

The first step of of the design process is to construct a 3D model of the device on a software, as is shown in Figure 3.2 (a). We used Autodesk Invertor in our study, other similiar software like Solidworks, ProE, and Catia, etc. can also be used. It is important to contruct the model with the film structure of each layer stacked, as shown in Figure 3.2 (b). In this way, the actual device fabrication using differently patterned PS film is already considered in the design process. It is also noticed from Figure 3.2 that two identical devices are embedded in a single chip. In this way

we fully utilized the resource and produced two testing devices from one fabrication period. Such technique is frequently used in our study, which have greatly increased the testing efficiency.

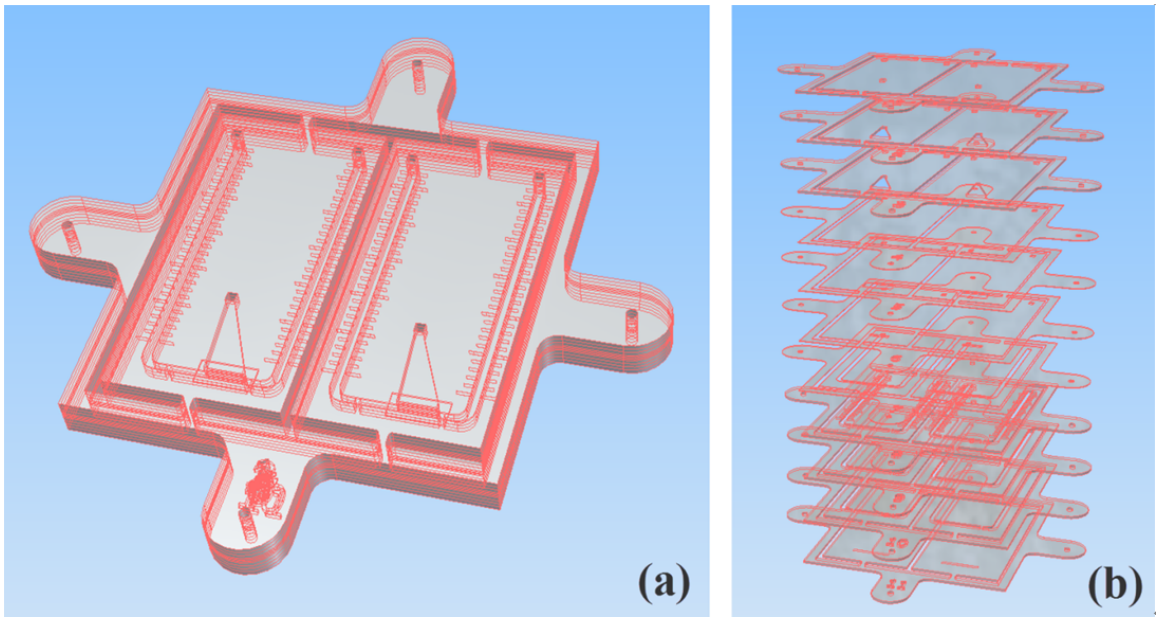

Fig. 3.2. Testing device design in 3D modeling software (a) 3D model of the testing device constructed in software environment. (b) Explosive view of the device model from 11 layers of patterned PS films.

After the full 3D model is constructed, a thorough check from the major view of the drawing is conducted to ensure its correctness, as is shown in Figure 3.3. The different layers of patterned PS films that established the 3D channel structure are demonstrated in the cross section view of Figure 3.3, the explosive view can be found in Figure 3.2 (b). From these pictures, one can understand the importance of constructing the full 3D model with different patterned layers. The model itself serves as a direct overview to guild the whole fabrication process that ensures minimum design flaws when it comes to the real device.

It is also noticed that a ruler with 1 mm resolution is embedded in the flow channel of the device as part of the design. This is for accurately measuring the meniscus movement in the inlet and outlet flow channel to measure the self-pumping rate.

Figure 3.4 shows an explosive view of the device design with 2D drawings of each layer's pattern. These 2D drawings are then ready to send to the digital cutter (FC2250-60 VC, Graphtec, Santa Ana, CA) to cut out each layer.

To prepare for the fabrication by the digital cutter, we need large sheets of PS film with different thickness according to the design. In the above device, two types of PS films are used, they are 125 μm and 50 μm thick. We also need to bring the PTFE nanoporous membrane (0.2 μm pore size, Sterlitech Corporation, Kent, WA) to be cut into the designed shape that is later to be assembled and embedded into the device, as is shown in the green part in Figure 3.3.

The last part of the preparation is about the Pt catalyst, which is the most important one. The Pt catalyst is the core of the catalytic reaction that drives the entire system for its functions, such as gas generation and self-circulation. It is fair to say that the performance of the catalyst directly decides the performance of the entire device. Therefore, we need to guarantee the quality of the Pt catalyst that we put into the device.

Previously, as shown in Section 2.1, our method to deposit Pt catalyst into the device was to use a spray gun to spray the catalyst solution onto a double-sided tape with a shadow mask. The tape was then assembled into the device, and the catalyst solution that had nano-sized Pt powder (20 percent) on carbon powder (80 percent) could be attached to the tape when cured because of the tape's adhesive surface. However, there were many limitation of this method. For example, since the Pt loading was low, the overall reaction rate was very limited. Because of the way it was implemented, the catalyst could not last very long, and the performance stability was not very high. More importantly, because of the carbon powder, the catalyst surface was very hydrophobic if not carefully treated, which was unfavorable for this device.

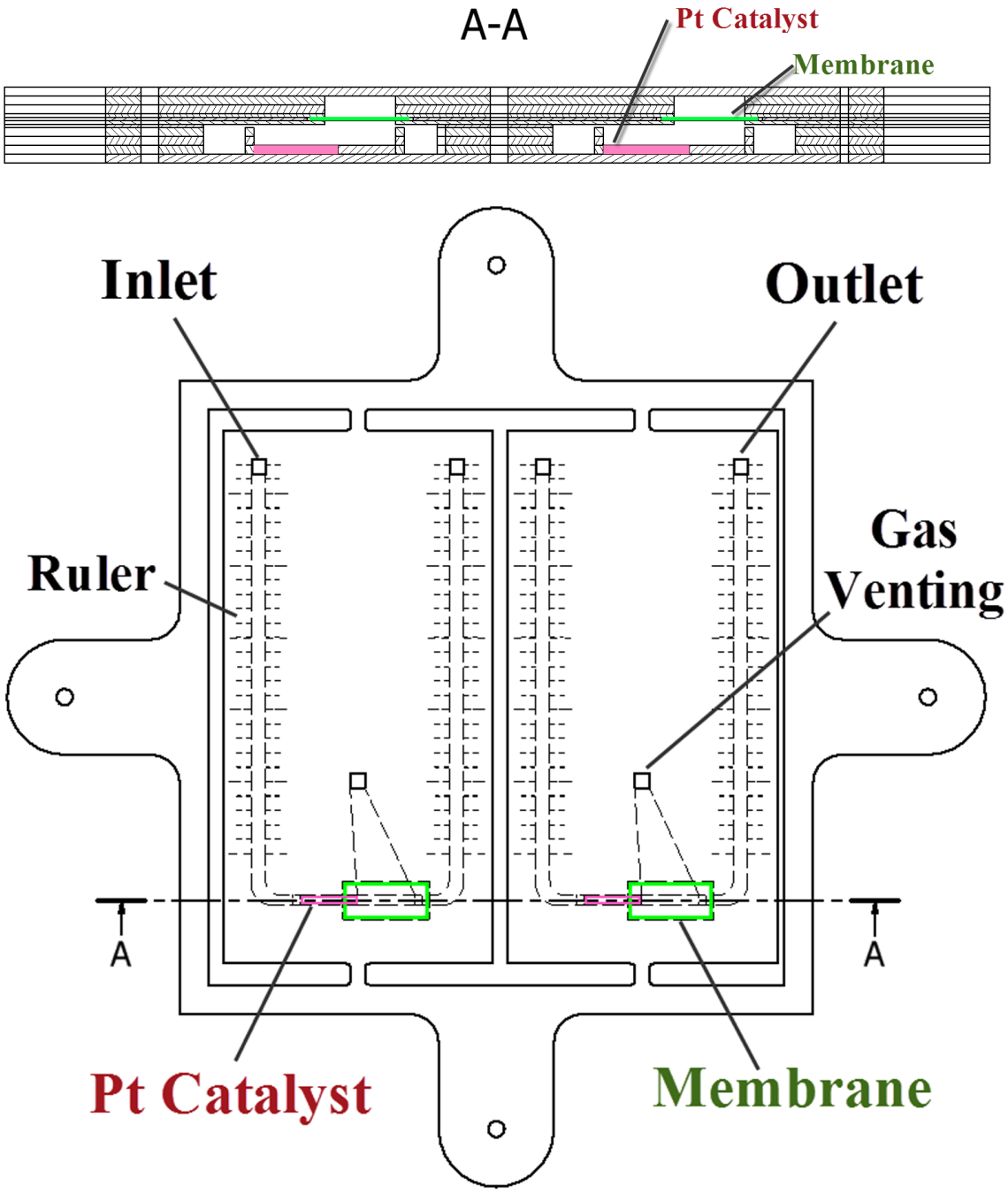

Fig. 3.3. Top view and cross section view of the testing device in design process.

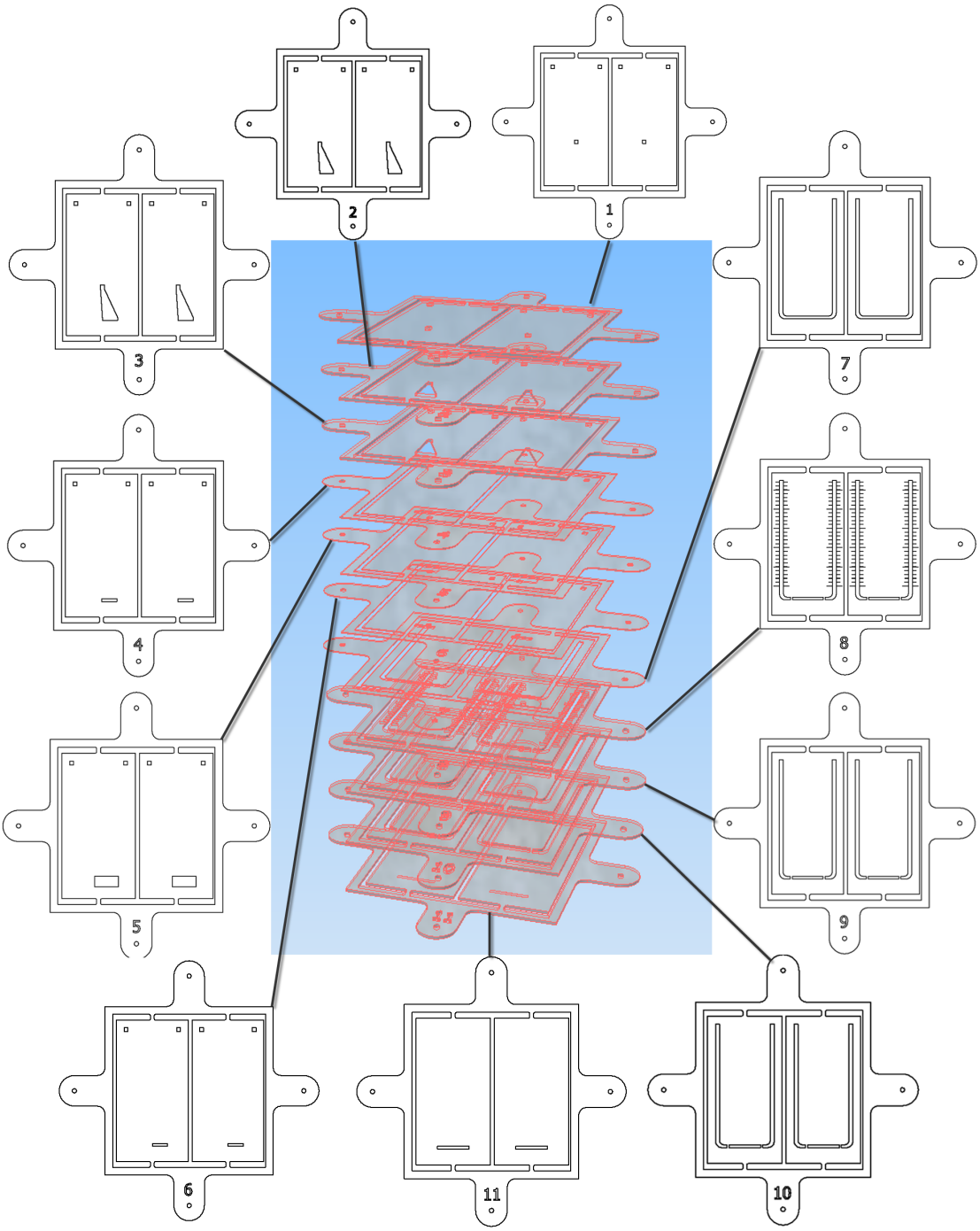

Fig. 3.4. Explosive view of the device design with 2D drawing of each layer.

Therefore, better catalyst is definitely needed for great performance improvement, and our answer is electroplating. We used Arbin Instrument as the power source to electroplate Pt on gold foil (10 μm thick). The current intensity was 0.1 A, gold electroplating area was about 1 cm^2, and the electroplating time was 55 s, the deposition density was measured and calculated to be 1.5 mg/cm^2. Highly uniform and reactive catalyst was achieved, and the electroplated catalyst is hydrophilic and stable for a long period of time [40]. It is noted that higher electroplating current can be applied on smaller area to achieve higher Pt deposition density.

The gold foil is attached on the double-sided tape when being electroplated with Pt. Then it can be attached to PS film with the other adhesive surface on the catalytic channel location, which can later be cut into the designed shape by the digital cutter, as is shown in the pink part in Figure 3.3.

After all the patterned PS films are acquired by the digital cutter, they can be fabricated into an integrated microfluidic gas generator by the thermopress bonding method described in Section 2.2. Then we attach plastic tubing connectors onto the device with epoxy. When it is fully cured, the device fabrication is complete and it is ready for testing, as is shown in Figure 3.5.

3.2 Testing Results and Discussions

With the process above, we have designed and fabricated a large amount of devices for channel optimization test. In the early stage of our test, we focused on seeking major understanding of the device working mechanism. After a series of preliminary tests, we have found suitable values for most of the dimensions in Figure 3.1. In the later part of the test, we redesigned our testing device and experimental method to find the delicate relationship between the channel height (H) and the gas generation performance, and therefore found the optimized channel dimensions for the gas generator.

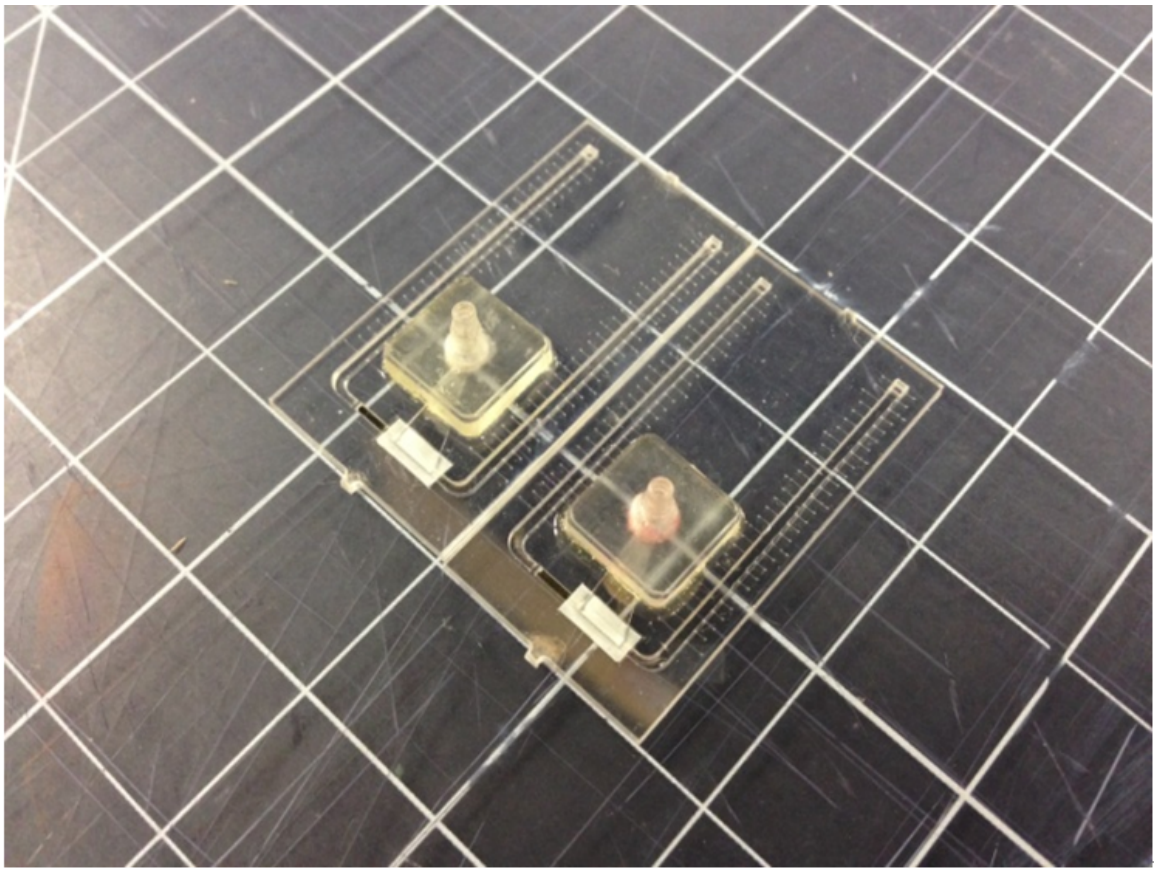

Fig. 3.5. Microfluidic gas generators from the PS based thermopress bonding method for dimension optimization test.

3.2.1 Preliminary Test

As is shown in Figure 3.1, the goal of our preliminary test is to decide some of the dimensions from experimental observation and experiences.

The first dimension to be determined is the width of the channel, which is not shown in the schematic. Since the self-pumping mechanism is capillary force driven, smaller channel dimension is generally desired. Considering the height of the channel should be the smaller dimension that determines the capillary force, the width of the channel is of secondary importance. Therefore, taken the digital cutter's resolution

and assembly alignment into consideration, we've set the width of the channel to be 0.7 mm.

The next dimension to be determined is the length of the reaction channel (L). Based on our experimental observation, especially the X-ray high speed image study in APS, Argonne Nation Laboratory (will be discussed in the next chapter). We believe the length of the channel should be around 5-10 mm, determined by the design requirement. Longer channel length means longer catalyst, which leads to higher gas generation rate. However, shorter L can bring higher chamber pressure, which is favorable for the venting and self-pumping mechanism (this will be discussed more in the following content). Therefore, based on our experimental results, a moderate value of 8 mm is chosen for general design of the microfluidic gas generator.

Now we decide the value for C and O. Because of the self-circulating mechanism explained in the introduction part, we believe the catalyst should cover only a large part of the reaction channel, and leave some part for the bubble's self-pumping activity. And also based on the observation using X-ray high speed imaging facility, we've found the right meniscus of the bubble being vented actually do not move very much. This means not much area is needed after the catalyst for the venting bubble. Considering the channel dimension scale we've set for total width and length, we've decided to let the length of catalyst (C) be 5 mm.

When the bubbles are generated in the reaction channel, as they grow, they tend to merge with each other into one large bubble. And when the edge of that bubble touches the venting membrane and gets vented, it will drag the rest part of the bubble to vent with it without breaking into smaller bubbles. This means if we design an overlapped area (O) between the catalyst and the membrane, the bubble generated on the catalyst is guaranteed to touch the venting membrane to be vented out. We don't want O to be too large compared to the length of the catalyst, which might disturb the bubble merging and dragging process that promotes the self-pumping. Therefore, we set O to be 1 mm.

Now we talk about the check valves, which is the crucial feature that decides the function of the device. The height of the check valve (t) needs to be small enough to hold the bubbles in the reaction channel, but it cannot be too small otherwise the liquid transport will be restricted that will result in poor performance. From the experiments and our fabrication capability, we used one layer of 50 μm patterned PS film to form the check valve, which means the height of the check valve, (t) is 50 μm. No gas bubble back flow has been observed with this check valve dimension, and the reactant pumping transport is smooth from experimental observation, which means this dimension for t is eligible for our current design.

In the introduction part, we mentioned that there was a problem of bubble blocking the check valve in our previous work that led to premature termination of the device. A careful revisit of Figure 1.5 shows us the reason. In our previous design, there were multiple check valves, each had significantly long check valve length compared to its height or width. And each of those check valves was like a long channel.

This explains why the device was susceptible to small bubbles that would block the check valve and shut down the device prematurely. Because no matter how small the check valve was, there would always be even smaller bubbles who inevitably found their way into the check valve. Since the length of the check valve was considerably larger than its channel diameter, each check valve was like a long channel to those bubbles. When the bubbles went into the check valve, it would be very hard for them to travel through the long channel to get out, thus the check valve channel was blocked.

The solution to this problem is simple: we design check valves with shorter length and use single-slot check valve instead of multiple check valve channels, like the image shown in Figure 2.13 (a). In this way, the small bubbles that get into the check valve will not be big enough to single-handedly block the entire slot-shaped check valve. And shorter check valve is also good for liquid transportation. Therefore, we set the length of the check to be 0.5 mm.

We have also designed testing devices with no second check valve (the right one) to study the importance of the symmetric check valve design. It turned out that if the second check valve disappeared, the bubbles generated in the reaction channel would most likely be pushed rightward into the outlet channel, rather than be vented out through the membrane. Therefore the self-circulating gas generator no long worked. From this finding, we realized the importance of the second check valve. Like the first check valve, it restricts the transportation of bubbles, therefore the generated gas bubbles are held in the reaction chamber. It is observed that the gas generation rate on Pt catalyst is very high, which means the gas bubbles generated in the small reaction chamber possess high pressure, especially with high concentration reactant solution. This reveals another major reason for self-pumping mechanism, because the pressure in the reaction channel is high enough to enable the venting of the bubble generated, which is why our device is able to work without the help of external negative pressure pump or internal positive pressure pump to help venting.

3.2.2 Channel Height Test

In the previous section, we have determined most of the dimensions from our reasonable judgments based on the experiments. There is one dimension left to be decided that we believe to be the most important dimension in the reaction channel, the height of the channel (H). Because this dimension directly determines the driving capillary force in the reaction channel, which decides the dynamics of the generated bubble.

In order to find the optimized channel height regarding the gas generating performance, we need to redesign the testing device different from previous ones. In the previous study, we designed and fabricated a different device for each different dimensional test. It was meant to find the suitable value range for the dimension, the exact value was then determined from a reasonable judgment based on our fabrication capability and design parameter. The limitation was that each time when a new

device was fabricated, there would be some minor uncontrollable factors due to the fabrication flaws that slightly changed the device, which was hard to avoid. These minor flaws were acceptable for the previous test, but not for the channel height test.

Because the channel height (H) is considered the most important dimension, a more delicate testing method is needed to rule out the interference of fabrication flaws. The answer is shown in Figure 3.6. Instead of fabricating a series of complete devices with different channel height for testing like in the previous study, we divide this testing device into 3 separate parts: the top part that has majority of the circulating channel of the device; the bottom part that has the Pt catalyst; and the replaceable middle parts with different thickness. These three parts can form a functional device when bonded together with double-sided tape mentioned in Section 2.1.

The beauty of this method is that we only fabricate one top part and one bottom part, and use them in all of our tests. Therefore we can expect uniform performance from the top channel and the Pt catalyst in all of our tests. By only changing the middle part that has different thickness, and bonding them together with double-sided tape, as is shown in Figure 3.6 (a,b), we have testable devices with only channel height (H) being the variable. In this way, we are able to achieve consistent testing result to unveil the delicate relationship between the channel height (H) and the gas generating performance.

In this study, we used the gas generation to evaluate the performance of the devices with different channel height. The test used 15 percent H_2O_2 to ensure high reaction rate that resulted in good venting pressure and high self-pumping rate. The collected gas generation rate plot is shown in Figure 3.7.

From Figure 3.7, we can observe substantial gas generation performance difference with different channel height. The channel height change step was 50 μm, which was the thickness of one layer of our thin PS film. The obvious gas generation rate drop in Figure 3.7 was due to short circulating channel for inlet and outlet, which created substantial resistance pressure when the outlet liquid was continuously pumped forward. The self-pumping rate of the devices were measured by the embedded ruler to

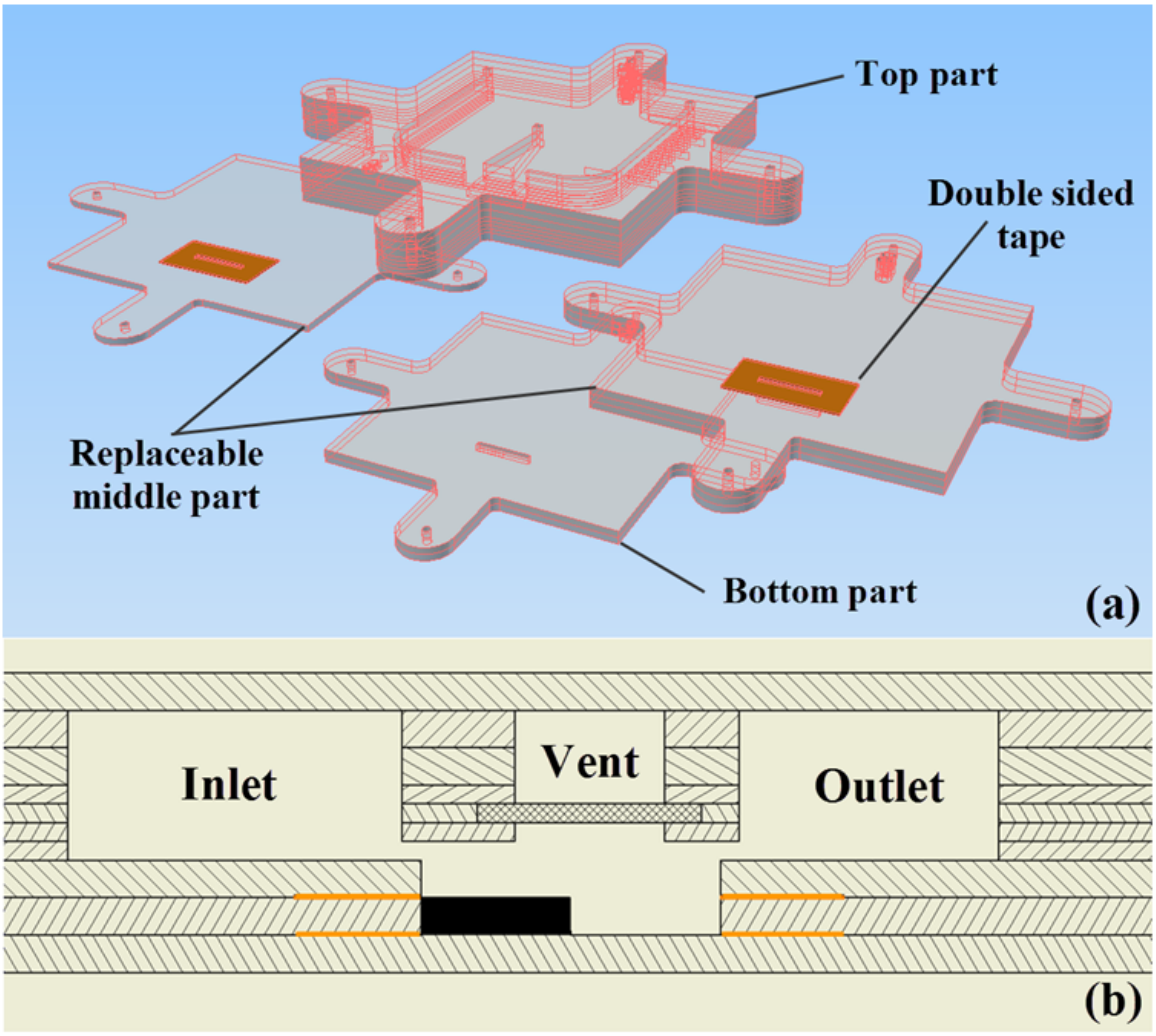

Fig. 3.6. Testing device for the channel height optimization. (a) Device overview with top part, bottom part, and replaceable middle part. (b) Device schematic showing the device bonded by orange double sided tapes.

be on the order of 0.1 μL/s, however, this is only an inaccurate rough result due to the significant self-reaction (15 percent H_2O_2) in the circulating channel that generated gas bubbles and affected the meniscus movement.

If we convert the gas generation curve into average gas generation rate and plot it with different channel height, we can have a more direct view of the relationship

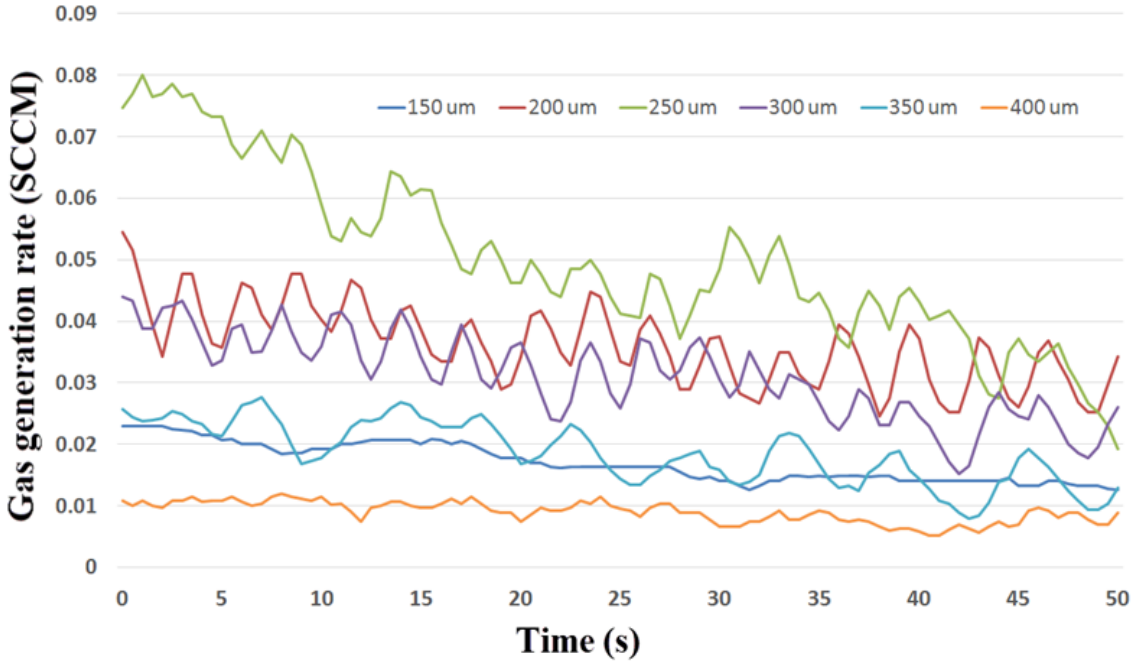

Fig. 3.7. Gas generation rate curves of testing devices with different channel height.

between the channel height and the gas generation performance, as is shown in Figure 3.8.

From Figure 3.8, we see can poor gas generation performance at both small channel height (150 μm) and large channel height (400 μm). This is because, when the channel height is small, the small volume of the reaction chamber made contact between reactant and catalyst very limited, which also resulted in limited gas venting rate. When the height of the reaction channel was too large, the pressure in the reaction channel would drop, this would significantly lower the gas venting rate, which resulted in poor gas generation rate. From the above figure, we can find the peak of the gas generating performance at channel height around 250 μm, which means this value is the optimized dimension for the reaction channel height (H).

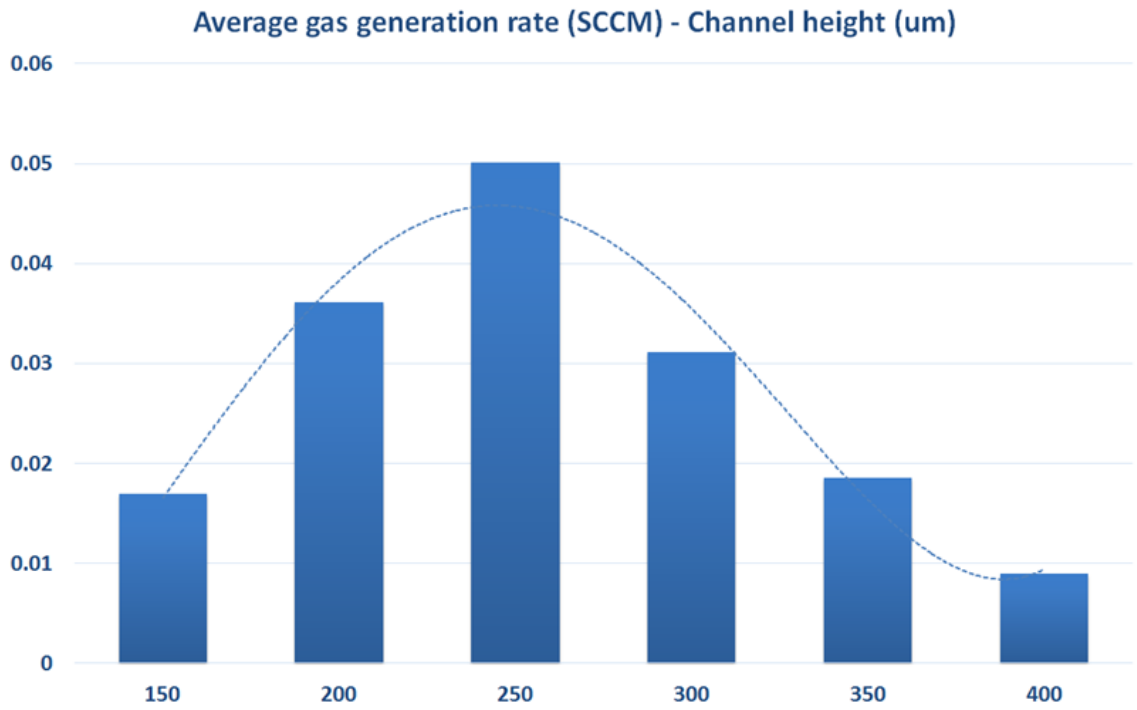

Fig. 3.8. Average gas generation rates with different channel height.

3.3 Conclusions

From the above results and discussions, we have determined all the dimensions in our reaction channel for optimal channel design, as is shown in Figure 3.9. Based on these dimensional values for a single reaction channel, we can design and fabricate microfluidic devices with multiple serial and parallel channels.

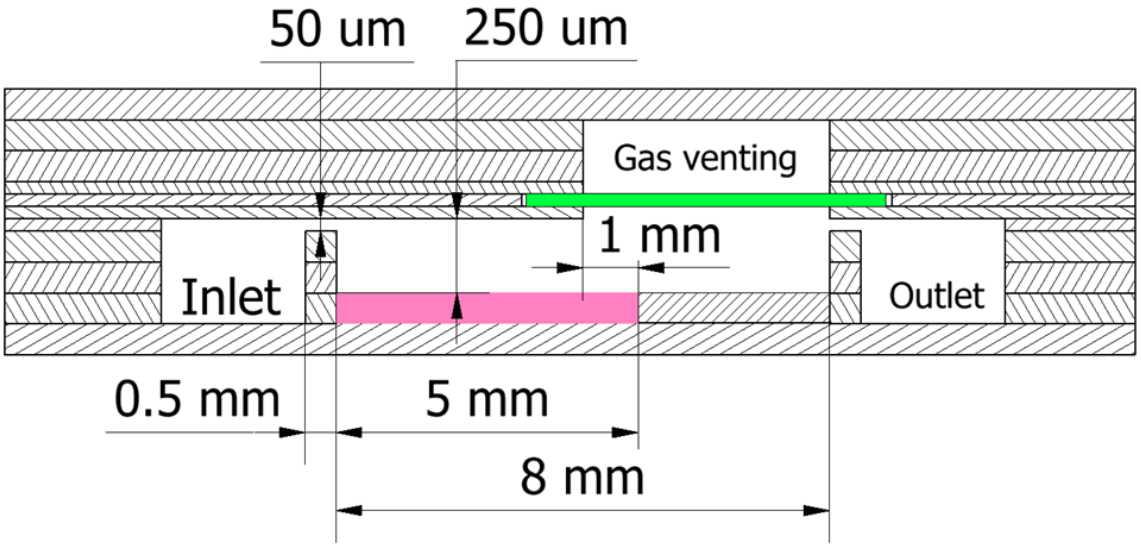

Fig. 3.9. Optimized channel design with complete dimensions.

4. HIGH SPEED IMAGE STUDY OF BUBBLE DYNAMICS

In order to gain more fundamental understanding about the dynamics in the self-circulating microfluidic gas generator, ultrafast synchrotron X-ray imaging facility at the Advanced Photon Source (APS), Argonne National Laboratory was used in this study. High speed images (100 KHz) were captured to observe and analyze the behavior of generated bubbles during the self-circulating and gas generating process in the device.

The driving core of our device is the Pt catalyst bed, which is widely used in chemistry related field to achieve controllable catalytic reactions [41]. Among them, gas generating reaction from aqueous reactant solution is particularly interesting, because this type of reaction involves three phase interaction. The reaction starts when the liquid state reactant contacts the solid state catalyst bed. As the gas bubbles generate on the catalyst surface, they block the reactant-catalyst interface and therefore slow down the reaction. The bubbles will gradually expand as the reaction continues, and merge into bigger bubbles that eventually stop the reaction by isolating the reactant from the catalyst.

We are particularly interested in the early stage of this gas generating catalytic reaction. By studying the captured high speed phase contrast X-ray images, we try to understand how the bubbles appear and grow from the catalyst bed, which we believe is meaningful for discovering potential applications in the area of chemistry, microfluidics, and biology, etc.

4.1 Experimental

The experiment was conducted at beamline 32 ID-B, Advanced Photon Source, Argonne National Laboratory. The high speed X-ray imaging facility allows direct observation inside the reaction flow cell. The experiment setup is illustrated in Figure 4.1 (a). X-ray comes from the source and goes through the reaction channel of the device after careful alignment, and is received by the high speed camera behind, as is shown in Figure 4.1 (b).

The testing device is a typical single-channel self-circulating self-regulating microfluidic gas generator, whose schematic is shown in Figure 4.1 (c). The working principle of the device has been illustrated in previous part of this thesis. The device's design process is the same as the testing devices illustrated in Section 3.1, and it was fabricated by the PS film based thermopress bonding method, as is introduced in Section 2.2. The device had similar channel dimension with the optimized dimensions discussed in the previous section. The area of interest of this high speed imaging test is the catalyst covered area, shown in Figure 4.1 (d), especially at the check valve region, where the self-pumping first happens.

One thing special about the testing device is that its longitudinal dimension of the reaction channel should be as small as possible, as is shown in Figure 4.1 (c). This can minimized the X-ray absorbance when it goes through the polymer based microfluidic device, therefore generating high speed phase contrast images with better resolution and sharpness. The generated image is shown in Figure 4.1 (e), it shows the phase contrast image with profiles of bubbles and other substances. This imaging technology allows us to directly observe inside the reaction channel on the cross section view during the self-pumping catalytic reaction, which is very helpful for its fundamental performance analysis and design improvement.

The experiment used 30 percent hydrogen peroxide (H_2O_2) as reactant solution, the catalytic reaction is triggered by contacting the Pt catalyst, and it produces water and oxygen gas. The reason why high concentration reactant is preferred is that it

allows more changes to take place within the limited 0.1s exposure time for high speed imaging. To avoid the influence of X-ray on H_2O_2, we have adjusted the X-ray dose beforehand and conducted a contrast test to make sure the H_2O_2 didn't have obvious self-reaction under existence of the X-ray.

4.2 Results and Discussions

4.2.1 Self-circulation Bubble Dynamics

During the experiment, we placed a self-circulating microfluidic gas generator as introduced above onto the platform for the X-ray high speed imaging test. Before the X-ray was activated, 30 percent H_2O_2 was already injected into the device from the inlet, which automatically turned the device on for oxygen generation. An external pump was connected to the venting tubing connector (the middle one) and was used to provide a negative sucking pressure of 1 psi for better venting.

This test allowed us to directly observe into the reaction channel during the self-pumping catalytic reaction, and the X-ray high speed imaging facility helped us to see what exactly was going on clearly and slowly. Figure 4.2 gives a demonstration about the testing results, our region of interests in the reaction channel was the area covered with the Pt catalyst, as is shown in Figure 4.2, which can also be found in Figure 4.1 (d). We were particularly interested in the check valve region and the venting membrane region. The image sequences in Figure 4.2, show us bubble dynamics that facilitated the self-circulation activity. From the image sequence at the check valve region (left), we can observe when the bubble that previously occupying the channel got dragged rightward due to the venting at the membrane region, new bubbles were quickly generated to fill the vacancy left by the old vented bubble. This dragging and filling activity happened periodically in the reaction channel that created continuous rightward pumping force.

These observed images have verified our proposal about the device's working principle, and it also provided important inspirations to improve the design. For example,

the image showed not much movement for the right meniscus at the venting membrane, which indicated shorter membrane length was actually needed in the device. Also, the catalytic reaction channel was longer than needed in the testing device. It seemed that shorter channel design would be better for the self-circulation.

4.2.2 High Speed Image Study of Bubble Generation

The reaction rate with 30 percent H_2O_2 solution on Pt catalyst bed is very high. As the self-circulating process is continuous, it is impossible to find the T = 0 point where the solution just came into the reaction channel and yet generates no bubbles. However, it is possible to find a relative early stage of the evolving process for a new round of bubble generation, as is shown in Figure 4.3. The image set demonstrates a typical evolving process for bubbles that were newly generated on the Pt catalyst bed. At the beginning, there were few big bubbles in the microchannel, and the contact between the reactant and the catalyst caused bubble generation reaction, that resulted in a layer of small bubbles on the surface of the catalyst bed, as is shown in Figure 4.3 (a,b). The emergence of these small bubbles from the catalyst bed was observed to be suddenly popped out (take place in 10 us), rather than expanded gradually from nothing. When the catalyst bed was covered with a layer of small bubbles whose diameter was less than 50 um, the bubbles began to gradually swell because of further catalytic reaction underneath them, as can be observed in Figure 4.3 (c). However, the major way for a bubble to evolve was by absorbing other bubbles and merging into a bigger one, as can be noticed in Figure 4.3 (c-e). This absorbing activity during the bubble developing process was particularly meaningful. By absorbing other bubbles and merging into a larger one, it also exposed the catalyst bed surface that was previously covered by the absorbed bubble, which made it possible for reactant to contact the catalyst bed that generated new bubbles. as is illustrated in Figure 4.3 (d-f). The bubble evolving process was therefore repeated, with newly generated small bubbles growing bigger and merging with other bubbles like the previous ones. The

early generated bubbles will be dominating and eventually merge into a single large bubble that filled the reaction channel, as it kept growing and absorbing other smaller bubbles, its right meniscus kept moving rightward, as is shown in Figure 4.3 (g), until it filled the entire reaction channel and touched the nanoporous venting membrane and got vented out, which would drag the whole bubble in the channel rightward and make room for a new round of bubble generation reaction, as is illustrated and explained in Figure 4.2.

Bubble Merging

Bubble merging composes the major dynamics of the evolving process. Figure 4.4 demonstrates an example of two similar-sized bubbles merging into a bigger one. The merging took place in 70 μs, even with high speed camera at a frame rate of 100 KHz (10 μs per frame), some details during the merging still escaped our observation. From Figure 4.4 at 0 μs, we can see two bubbles whose diameter was less than 100 μm were side by side growing independently in the reaction channel. At this moment, they were about to contact each other. The merging of the two bubbles took place in a very short period of time (less than 10 μs which was the resolution for 100 KHz high speed images), and in the next frame after 10 μs, the two bubble have formed the joint meniscus, with an arch shape in the middle. Since the bubble merging happened very fast, and with the merging of two bubbles into one bubble, the peripheral parameters of the bubbles also needed to change accordingly, including the total surface area and volume of the bubbles. This sudden motion provided relative high kinetic energy for the bubbles, therefore enabling a series of oscillating movement for the merged bubble, which can be observed at 20 μs, 30 μs, 40 μs frame points. It is noticed that each of these frame, even though only has short time step of 10 μs, possesses obvious bubble shape difference. This indicates high kinetic energy of the bubble after the merging, and the energy was dissipated to the peripheral environment through the bouncing-like activity. After about 50 μs after the merging of the two bubbles, the

merged bubble's oscillating movement started to calm down, as is shown in Figure 4.4 at 50 μs, 60 μs, 70 μs time frame. The merged bubble eventually restored the spherical shape which had minimum surface area. The whole merging process was completed in 70 μs, which was a considerably short period of time. During the merging process, bubble meniscus movement have been captured using 100 KHz high speed X-ray phase contrast imaging facility with a time step of 10 μs. However, detailed merging information between two consecutive time frames (in 10 μs) still escaped our observation.

Figure 4.5 demonstrates another merging scenario where a bigger bubble absorbed a smaller bubble. This example can be related to the discussion on Figure 4.3 (e,f). In a typical bubble developing process, the major way for a large bubble to grow and expand is by absorbing the nearby smaller bubbles, as is shown in Figure 4.5 at 0 μs. It is noticed that the bigger bubble and the smaller bubble had an obvious overlapping area from the image. This is because the reaction channel in the experiment had a channel width of 700 μm, which was significantly larger than its height that was only about 200 μm. The bubbles were on different longitudinal planes, which is why they appeared to have touched each other without merging. At 10 μs time point, as the bubbles kept growing, their meniscus began to contact and initiated the merging. The arch shape meniscus can be observed between the two bubbles at the merging region, as is shown in 20 μs, 30 μs. And the merged bubble had similar bouncing movement like the previous one, as is shown in Figure 4.5 (40 μs - 80 μs), and eventually restored calm at 90 μs. Different from the previous case shown in Figure 4.4, due to the bubble size difference, the merging process did not exhibit obvious bubble shape oscillating activity. The whole merging activity was completed in 90 μs, which was also very fast and had similar speed with the previous one. This kind of fast speed merging activity formed the majority of the bubble development process in the microchannel on the Pt catalyst bed. Since the merging is capable of activating high kinetic energy in a very short period of time, it is believed that further study on this subject has

the potential to bring applications in a variety of fields, like microfluidics, chemistry, physics, and bio-medical, etc.

Bubble Growth

It is understood that the growth of a bubble on the catalyst bed is largely dependent on merging with other bubbles, as well as the self-expanding from the ongoing catalytic reaction. Therefore, a bubble's growing process can be discrete and unsmooth. To understand the relationship between growth rate and reaction time, we picked up some independent growing bubbles and tracked their volume with time, like the one shown in Figure 4.6. It is noted that all bubbles here were in growing stage before they were big enough to reach the top of the channel, therefore they were assumed to be part of spherical for volume calculation.

To plot the volume change of the bubble with time, we first need to measure the diameter of the bubble from the TIFF format 100 KHz high speed images. And then we measure the contact length of the bubble contacting the Pt catalyst surface, which is the diameter of the bubble's contacting circular area. With that, we can calculate the semi-spherical bubble's contact area and volume, and therefore plot them with time.

Figure 4.7 shows the growth rate of bubble's diameter during the developing process, from the plot, we can find good linear relationship between the bubble diameter and time.

Similar linear relationship between the contact area of the bubble and time can be found in Figure 4.8. It is noticed that large oscillating has been observed in the growth rate curve for the bubble's contact area. This is because the bubble will have minor yet constant bouncing activity during its evolving process, especially when it absorbs another bubble that releases internal kinetic energy. The bouncing will cause dramatic change in the bubble's contacting area with the Pt catalyst bed, which explains the big oscillating in plot of Figure 4.8.

With the growth rate of the bubble's diameter and contacting area found to be linear with time, we then move on to plot the growth rate of bubble's volume, which is an overall assessment of the bubble's growth rate. As is shown in Figure 4.9, the growth rate of bubble's volume increases with time, as the bubble becomes larger, it has a higher self-reaction rate due to larger catalyst contact area. And it also has access to more bubbles to absorb due to its increased surface area, which leads to higher growth rate. The increasing trend matches exponential curve, or polynomial curve, which can be expected from the linear growth rate of bubble's diameter.

4.3 Conclusions

The high speed X-ray image study in this chapter provided us direct observation into the reaction channel of our self-circulating microfluidic gas generator during the catalytic reaction. From the phase contrast images, we have observed the expected dynamic bubble behavior that verified our device's working principle. It also provided insights to further optimize the channel design by shortening the length of the catalyst covered channel and the venting membrane. Better self-pumping performance and even more compact design are to be expected due to the testing results.

The 100 KHz high speed images also gives us useful information about the dynamics of bubble development on a catalyst bed, which includes detailed captured images about the growth and merging of the bubbles. We have found linear growth rate for a bubble's diameter and its contacting area with the catalyst during its developing process, and exponential growth rate for bubble's volume. These findings have the potential to bring more applications in the field of physics, chemistry, microfluidics, and biology, etc.

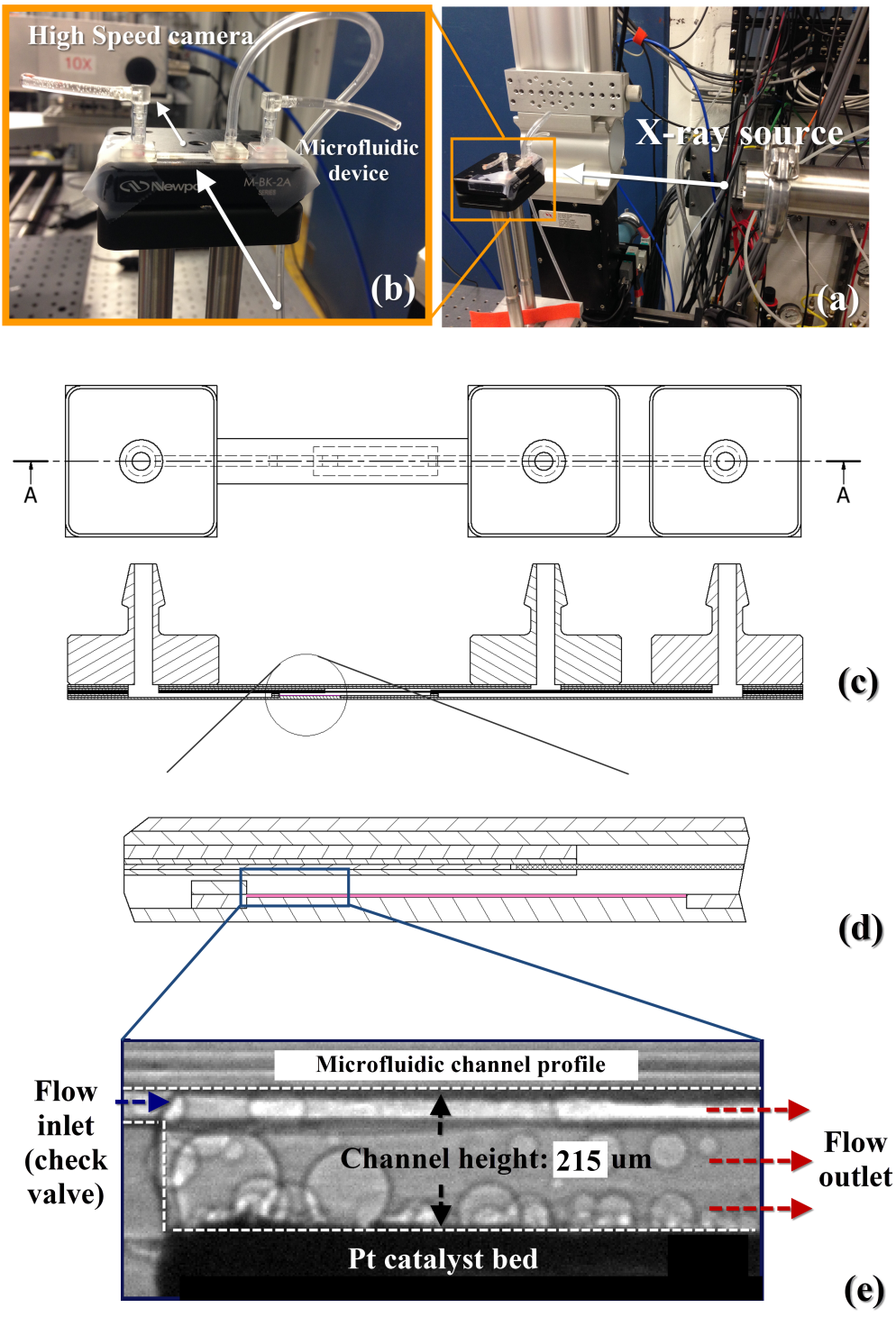

Fig. 4.1. (a, b) X-ray high speed imaging experiment setup (c) Testing device schematic (d) Detail view of the reaction channel (e) Phase contrast image in the check valve region.

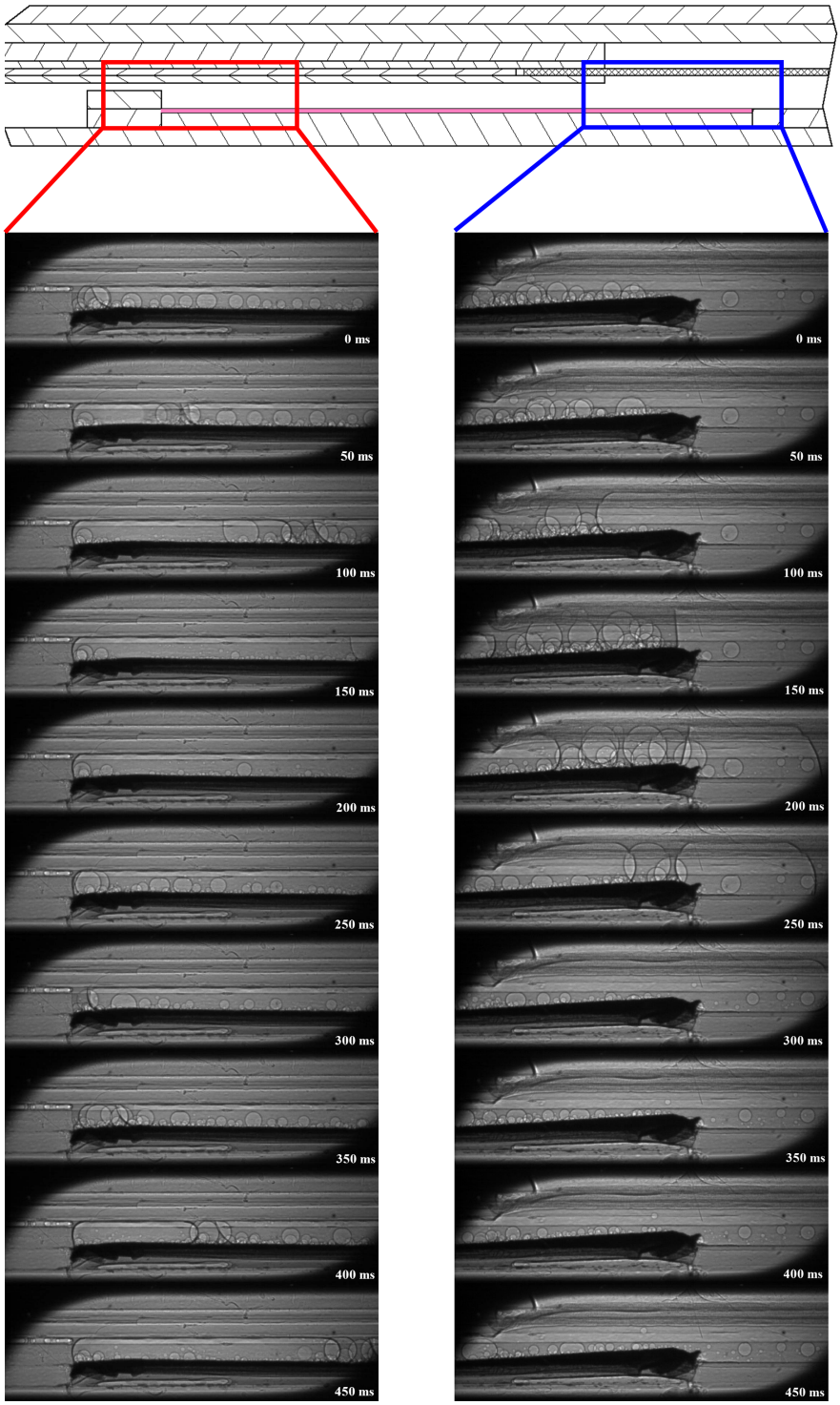

Fig. 4.2. X-ray image sequences showing the bubble dynamics at the check valve and venting membrane region during the self-pumping catalytic reaction.

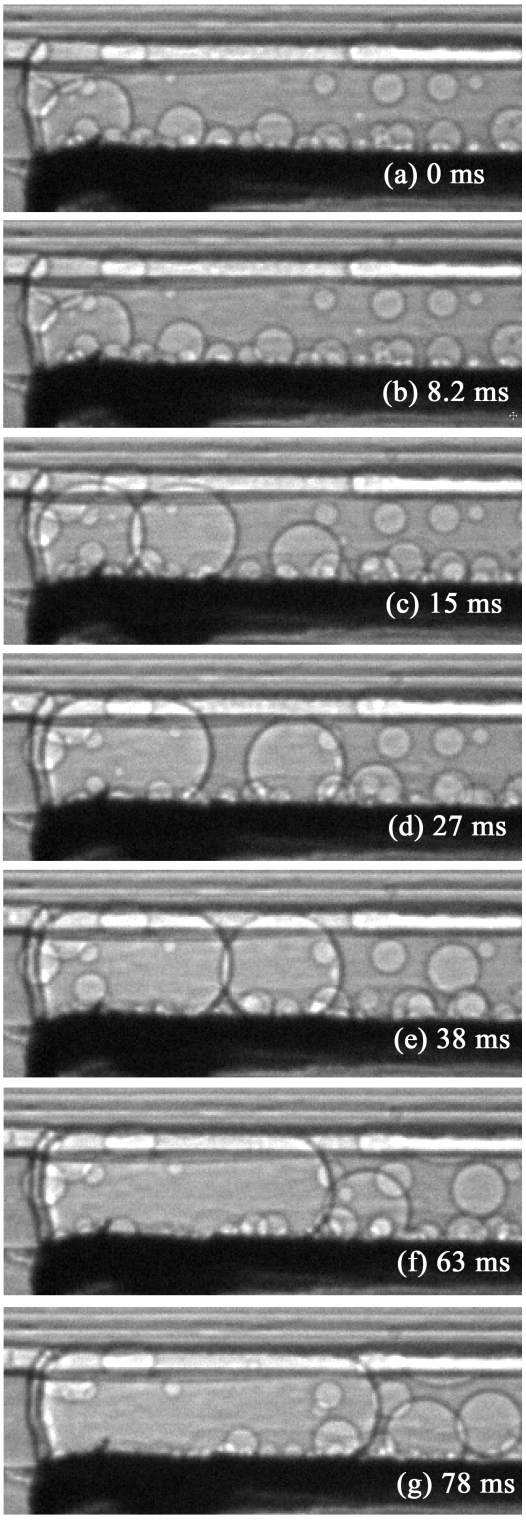

Fig. 4.3. Bubble developing process with 30 percent H_2O_2 on Pt catalyst bed in 78 ms.

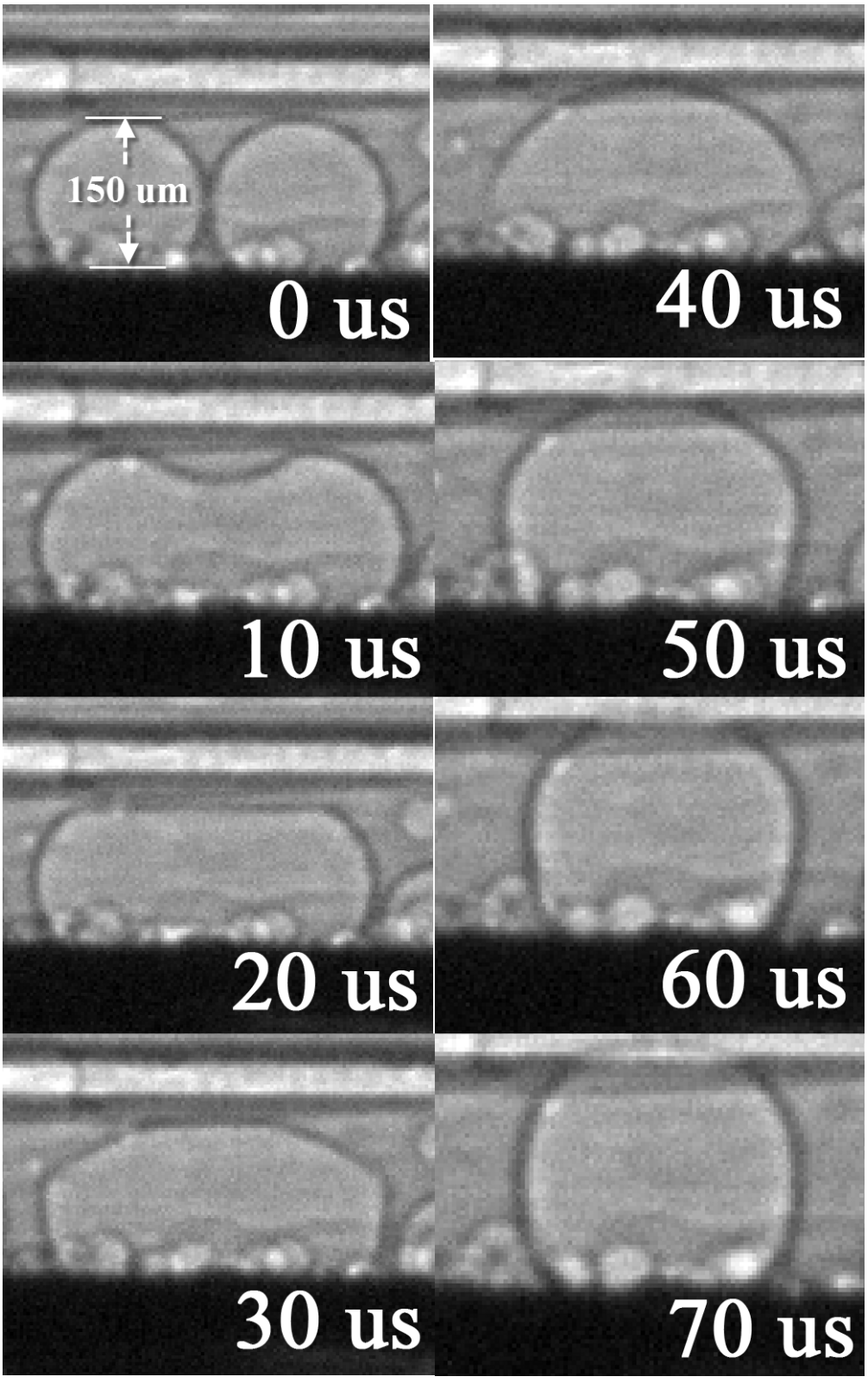

Fig. 4.4. Two bubbles of similar size merging into a bigger one in 70 μs.

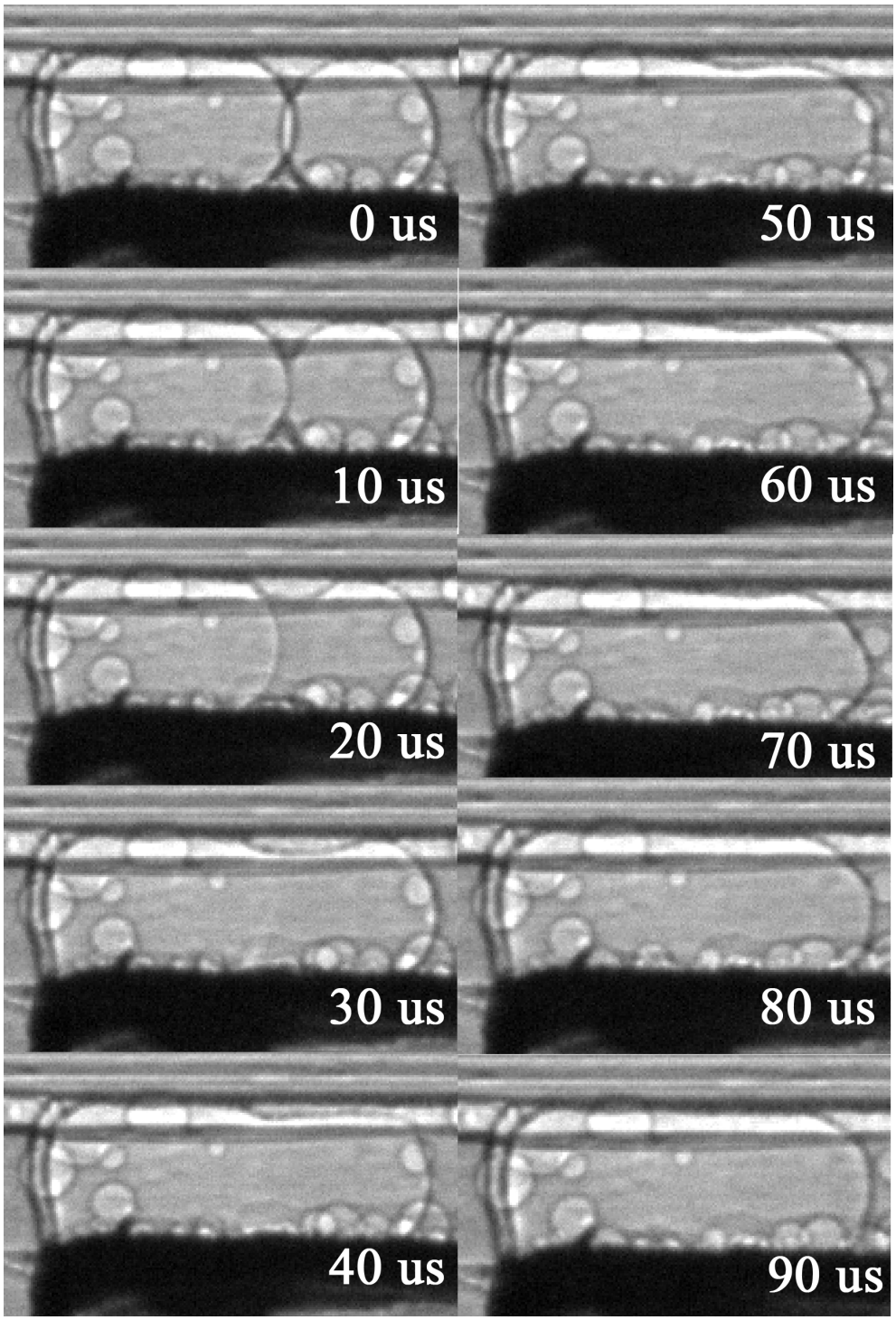

Fig. 4.5. A larger bubble absorbing a smaller bubble, the whole process completed in 90 μs.

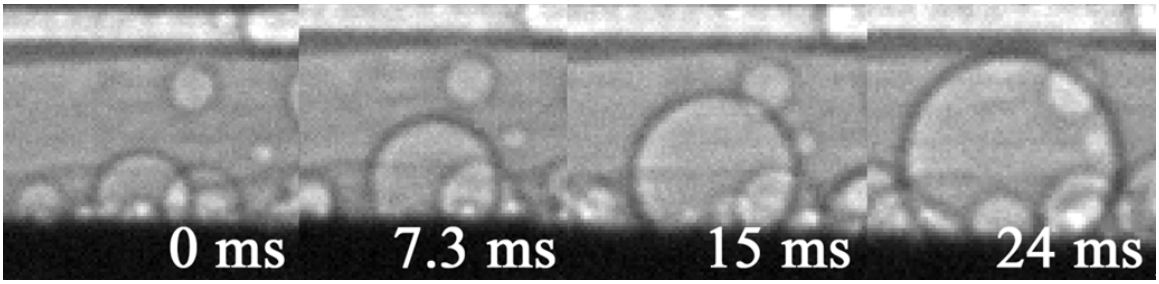

Fig. 4.6. The growth of a particular bubble with measurable volume as growth rate on real time scale.

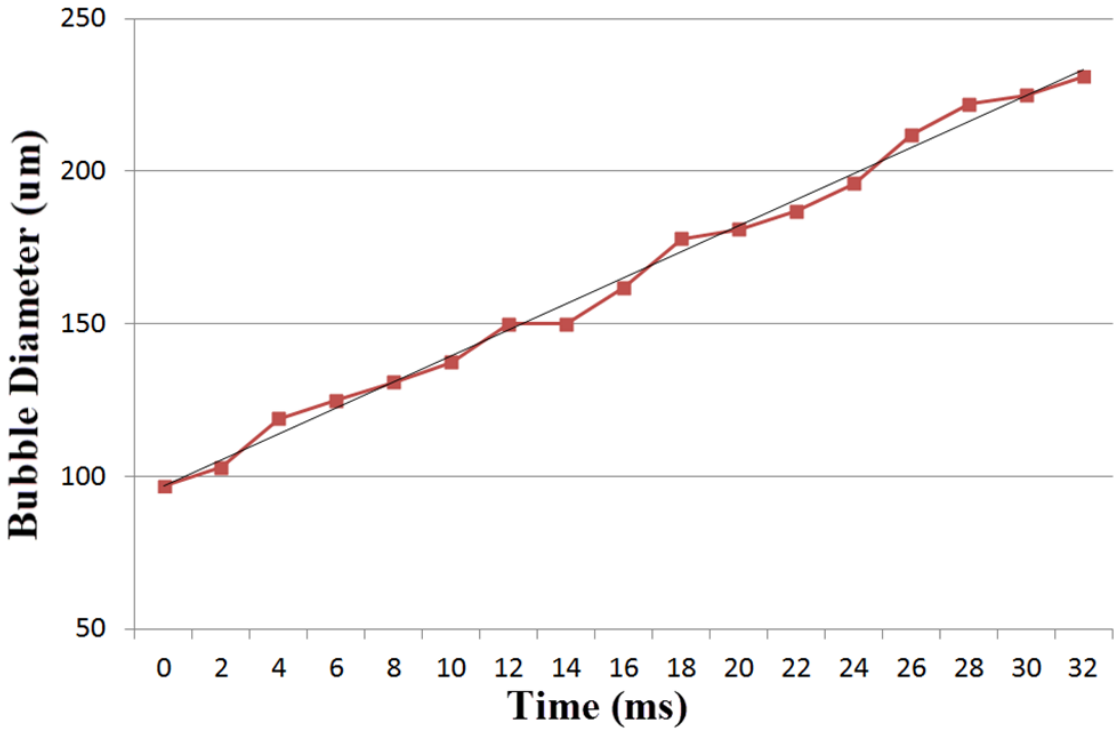

Fig. 4.7. Plot of bubble's growth rate, bubble diameter-time.

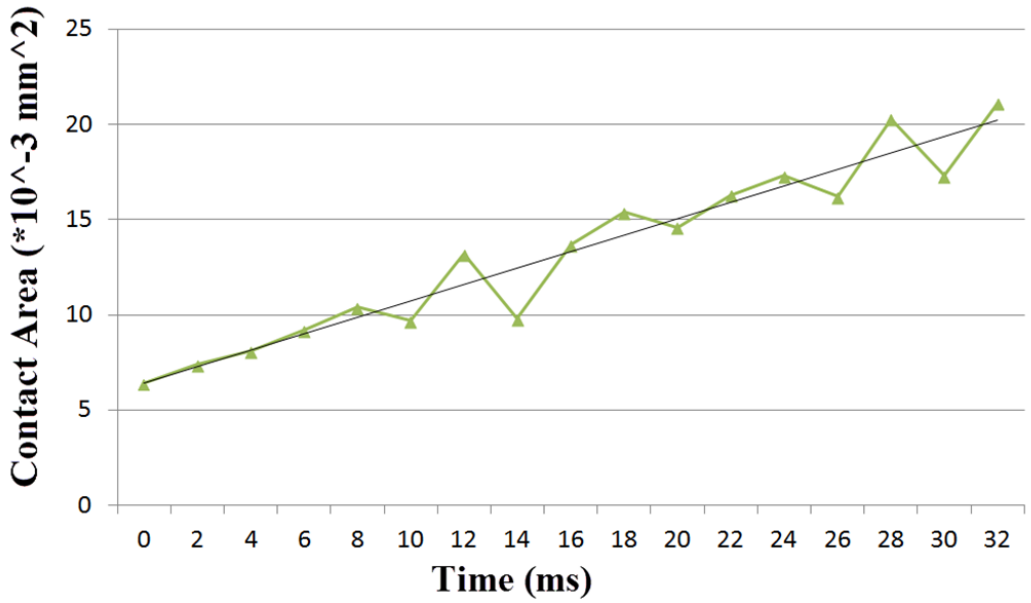

Fig. 4.8. Plot of bubble's growth rate, contact area-time.

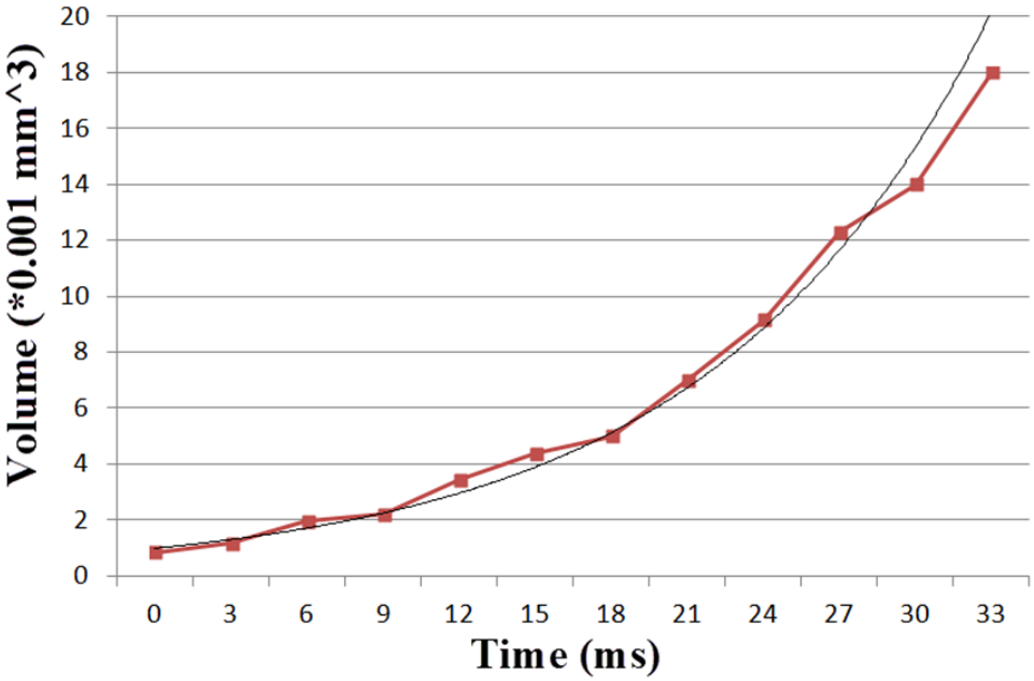

Fig. 4.9. Plot of bubble's growth rate, volume-time.

5. CONCLUSIONS AND RECOMMENDATIONS

5.1 Conclusions

This thesis has used experimental method to improve the performance of the self-circulating self-regulating microfluidic gas generation system by finding the optimal dimensions for the channel structure design.

In order to do that, a microfluidic device fabrication method that is time and cost efficient with relatively high resolution is needed. Therefore, the major part of this thesis has been focused on the microfabrication method development. There are two microfabrication methods that have been developed, including the double-sided tape-based method, and the more advanced PS film-based microfabrication method.

Next, based on the PS film microfabrication method, the article has demonstrated a large amount of carefully designed experiments about the microchannel dimensional test. Based on the collected gas generation rate data, the testing devices with different channel dimension parameters have been evaluated. In this way, an optimized microfluidic channel dimension under certain preliminary settings has been found.

The last part of this thesis has illustrated the study of bubble dynamics using the high speed X-ray imaging facility in APS, Argonne National Laboratory. Ultrafast phase contrast images were captured during the catalytic reaction inside the microchannel. These image data helped us to establish a more fundamental understanding about the working mechanism of the self-circulating microfluidic gas generator, which in turn contributed to the channel optimization study.

5.2 Future Work Recommendations

Based on what we have achieved, the followings are given as a recommendation for future work.

1. The effect of serial and parallel channels in a microfluidic gas generator should be investigated.

2. Further study on circulating channel structure design should be conducted to establish better internal pressure balance, which is crucial for the performance sustainability of the self-circulating gas generator.

3. A fully integrated and independent device with optimized structure and multiple channel design should be developed.

LIST OF REFERENCES

LIST OF REFERENCES

[1] K. Cowey, K. Green, G. Mepsted, and R. Reeve, "Portable and military fuel cells," *Current Opinion in Solid State and Materials Science*, vol. 8, no. 5, pp. 367–371, 2004.

[2] M. Varady, L. McLeod, J. Meacham, F. Degertekin, and A. Fedorov, "An integrated mems infrastructure for fuel processing: hydrogen generation and separation for portable power generation," *Journal of Micromechanics and Microengineering*, vol. 17, no. 9, p. S257, 2007.

[3] P. Muthukumar, M. P. Maiya, and S. S. Murthy, "Experiments on a metal hydride-based hydrogen storage device," *International Journal of Hydrogen Energy*, vol. 30, no. 15, pp. 1569–1581, 2005.

[4] L. Zhu, V. Swaminathan, B. Gurau, R. Masel, and M. Shannon, "An onboard hydrogen generation method based on hydrides and water recovery for micro-fuel cells," *Journal of power sources*, vol. 192, no. 2, pp. 556–561, 2009.

[5] D. Gervasio, S. Tasic, and F. Zenhausern, "Room temperature micro-hydrogen-generator," *Journal of Power Sources*, vol. 149, pp. 15–21, 2005.

[6] K. Hoeppner, R. Hahn, H. Reichl, M. Esashi, and S. Tanaka, "Fabrication and evaluation of a nabh4 hydrogen microreactor assembled by triple stack glass bonding," *Catalyst*, vol. 4, p. 3, 2009.

[7] M. Strizki and S. Shah, "Self-regulating hydrogen generator," Sept. 6 2005. US Patent 6,939,529.

[8] D. D. Meng *et al.*, "Micropumping of liquid by directional growth and selective venting of gas bubbles," *Lab on a Chip*, vol. 8, no. 6, pp. 958–968, 2008.

[9] D. D. Meng and C. Kim, "An active micro-direct methanol fuel cell with self-circulation of fuel and built-in removal of co 2 bubbles," *Journal of Power Sources*, vol. 194, no. 1, pp. 445–450, 2009.

[10] S. Moghaddam, E. Pengwang, R. I. Masel, and M. A. Shannon, "A self-regulating hydrogen generator for micro fuel cells," *Journal of Power Sources*, vol. 185, no. 1, pp. 445–450, 2008.

[11] N. Paust, C. Litterst, T. Metz, M. Eck, C. Ziegler, R. Zengerle, and P. Koltay, "Capillary-driven pumping for passive degassing and fuel supply in direct methanol fuel cells," *Microfluidics and nanofluidics*, vol. 7, no. 4, pp. 531–543, 2009.

[12] L. Zhu, N. Kroodsma, J. Yeom, J. Haan, M. Shannon, and D. Meng, "An on-demand microfluidic hydrogen generator with self-regulated gas generation and self-circulated reactant exchange with a rechargeable reservoir," *Microfluidics and nanofluidics*, vol. 11, no. 5, pp. 569–578, 2011.

[13] L. Zhu, D. Meng, N. Kroodsma, J. Yeom, and M. Shannon, "An integrated microfluidic self-regulating and self-circulating hydrogen generator for fuel cells," in *Solid-State Sensors, Actuators and Microsystems Conference, 2009. TRANSDUCERS 2009. International*, pp. 652–655, IEEE, 2009.

[14] E. W. Young, E. Berthier, D. J. Guckenberger, E. Sackmann, C. Lamers, I. Meyvantsson, A. Huttenlocher, and D. J. Beebe, "Rapid prototyping of arrayed microfluidic systems in polystyrene for cell-based assays," *Analytical chemistry*, vol. 83, no. 4, pp. 1408–1417, 2011.

[15] P. K. Yuen and M. E. DeRosa, "Flexible microfluidic devices with three-dimensional interconnected microporous walls for gas and liquid applications," *Lab on a Chip*, vol. 11, no. 19, pp. 3249–3255, 2011.

[16] S.-Y. Teh, R. Lin, L.-H. Hung, and A. P. Lee, "Droplet microfluidics," *Lab on a Chip*, vol. 8, no. 2, pp. 198–220, 2008.

[17] P. S. Dittrich and A. Manz, "Lab-on-a-chip: microfluidics in drug discovery," *Nature Reviews Drug Discovery*, vol. 5, no. 3, pp. 210–218, 2006.

[18] P. Gravesen, J. Branebjerg, and O. S. Jensen, "Microfluidics-a review," *Journal of Micromechanics and Microengineering*, vol. 3, no. 4, p. 168, 1993.

[19] D. J. Beebe, G. A. Mensing, and G. M. Walker, "Physics and applications of microfluidics in biology," *Annual review of biomedical engineering*, vol. 4, no. 1, pp. 261–286, 2002.

[20] H. A. Stone, A. D. Stroock, and A. Ajdari, "Engineering flows in small devices: microfluidics toward a lab-on-a-chip," *Annu. Rev. Fluid Mech.*, vol. 36, pp. 381–411, 2004.

[21] T. M. Squires and S. R. Quake, "Microfluidics: Fluid physics at the nanoliter scale," *Reviews of modern physics*, vol. 77, no. 3, p. 977, 2005.

[22] D. C. Duffy, J. C. McDonald, O. J. Schueller, and G. M. Whitesides, "Rapid prototyping of microfluidic systems in poly (dimethylsiloxane)," *Analytical chemistry*, vol. 70, no. 23, pp. 4974–4984, 1998.

[23] J. R. Anderson, D. T. Chiu, H. Wu, O. J. Schueller, and G. M. Whitesides, "Fabrication of microfluidic systems in poly (dimethylsiloxane)," *Electrophoresis*, vol. 21, pp. 27–40, 2000.

[24] P. Pal and K. Sato, "Various shapes of silicon freestanding microfluidic channels and microstructures in one-step lithography," *Journal of Micromechanics and Microengineering*, vol. 19, no. 5, p. 055003, 2009.

[25] P. Kim, K. W. Kwon, M. C. Park, S. H. Lee, S. M. Kim, and K. Y. Suh, "Soft lithography for microfluidics: a review," 2008.

[26] J. C. McDonald and G. M. Whitesides, "Poly (dimethylsiloxane) as a material for fabricating microfluidic devices," *Accounts of chemical research*, vol. 35, no. 7, pp. 491–499, 2002.

[27] R. Shatford and V. Karanassios, "Microplasma fabrication: from semiconductor technology for 2d-chips and microfluidic channels to rapid prototyping and 3d-printing of microplasma devices," in *SPIE Sensing Technology+ Applications*, pp. 91060H–91060H, International Society for Optics and Photonics, 2014.

[28] P. K. Yuen and V. N. Goral, "Low-cost rapid prototyping of flexible microfluidic devices using a desktop digital craft cutter," *Lab on a Chip*, vol. 10, no. 3, pp. 384–387, 2010.

[29] Y. Fan, H. Li, Y. Yi, and I. G. Foulds, "Pmma to polystyrene bonding for polymer based microfluidic systems," *Microsystem technologies*, vol. 20, no. 1, pp. 59–64, 2014.

[30] L. Tang and N. Y. Lee, "A facile route for irreversible bonding of plastic-pdms hybrid microdevices at room temperature," *Lab on a Chip*, vol. 10, no. 10, pp. 1274–1280, 2010.

[31] F. Reymond, J. S. Rossier, and H. H. Girault, "Polymer microchips bonded by o2-plasma activation," *Electrophoresis*, vol. 23, pp. 782–790, 2002.

[32] C.-W. Tsao and D. L. DeVoe, "Bonding of thermoplastic polymer microfluidics," *Microfluidics and Nanofluidics*, vol. 6, no. 1, pp. 1–16, 2009.

[33] Y. Wang, J. Balowski, C. Phillips, R. Phillips, C. E. Sims, and N. L. Allbritton, "Benchtop micromolding of polystyrene by soft lithography," *Lab on a Chip*, vol. 11, no. 18, pp. 3089–3097, 2011.

[34] J. M. Grace and L. J. Gerenser, "Plasma treatment of polymers," *Journal of Dispersion Science and Technology*, vol. 24, no. 3-4, pp. 305–341, 2003.

[35] C.-S. Chen, D. N. Breslauer, J. I. Luna, A. Grimes, W.-c. Chin, L. P. Lee, and M. Khine, "Shrinky-dink microfluidics: 3d polystyrene chips," *Lab on a Chip*, vol. 8, no. 4, pp. 622–624, 2008.

[36] Ö. Vallin, K. Jonsson, and U. Lindberg, "Adhesion quantification methods for wafer bonding," *Materials Science and Engineering: R: Reports*, vol. 50, no. 4, pp. 109–165, 2005.

[37] A. Larsson and H. Dérand, "Stability of polycarbonate and polystyrene surfaces after hydrophilization with high intensity oxygen rf plasma," *Journal of colloid and interface science*, vol. 246, no. 1, pp. 214–221, 2002.

[38] Y. K. Suh and S. Kang, "A review on mixing in microfluidics," *Micromachines*, vol. 1, no. 3, pp. 82–111, 2010.

[39] A. Bhattacharyya and C. M. Klapperich, "Mechanical and chemical analysis of plasma and ultraviolet–ozone surface treatments for thermal bonding of polymeric microfluidic devices," *Lab on a Chip*, vol. 7, no. 7, pp. 876–882, 2007.

[40] K. Kitada and S. Yarita, "Platinum electroforming and platinum electroplating," June 25 1996. US Patent 5,529,680.

[41] L. Ma and D. Trimm, "Alternative catalyst bed configurations for the autothermic conversion of methane to hydrogen," *Applied Catalysis A: General*, vol. 138, no. 2, pp. 265–273, 1996.